THICKNESS AND STACKING SEQUENCE DETERMINATION OF 1T-TANTALUM DISULFIDE USING SCANNING TRANSMISSION ELECTRON MICROSCOPY

A Thesis

Presented to the Faculty of the Graduate School

of Cornell University

In Partial Fulfillment of the Requirements for the Degree of

Master of Science

By

Pengzi Liu

August 2015

ABSTRACT

The layered transition metal dichalcogenide (TMD), 1T-tantalum disulfide (1T-TaS_2) exhibits a range of electronic properties when cooled down, including phase transitions associated with charge-density-waves (CDWs), metal-insulator transitions as well as superconductivity upon doping or high pressure. The CDW phase transitions can be modulated by the thickness of 1T-TaS_2. To understand the material's potential for electronic applications it is therefore important to identify the dimension and atomic layer stacking of 1T-TaS_2 samples with both accuracy and precision. In this work, our goal is to develop a reliable method to extract the thickness and stacking sequence of 1T-TaS_2 directly from experimentally recorded images.

High-angle annular dark field (HAADF) scanning transmission electron microscopy (STEM) is a powerful method to image materials with atomic resolution. However, considering the two-dimensional nature of projected HAADF-STEM images, we choose the technique of convergent-beam electron diffraction (CBED) performed with atomically small electron beams from STEM. We show that combining experimental and simulated CBED patterns with rich information in the third-direction (i.e. thickness and stacking sequence) is an effective approach to study the structures of layered dichalcogenides.

I will discuss the development of a method to extract the thickness and stacking sequence of exfoliated 1T-TaS_2 layered structures directly from experimental CBED

patterns and STEM images by comparison with simulation results. Starting with multislice simulations of both HAADF-STEM images and CBED patterns for 1T-TaS_2 thickness and stacking sequence, I will demonstrate the influence on the image contrast. By comparison of these results with experimental data I show that the thickness of 1T-TaS_2 with simple stacking (all-A stacking) can be determined with a ± 1 unit cells uncertainty. Variations in the symmetry and the intensity distribution in CBED patterns can be used to distinguish simple all-A (AA….A) stacking from other stacking. Finally, I will briefly discuss the limitations of this method and future work.

BIOGRAPHICAL SKETCH

Pengzi Liu was born in Handan, China in 1991. She started her physics studies at the Harbin Institute of Technology, China in 2009. At her sophomore year, she went to the University of Science and Technology of China as an exchange student for one semester. And she joined X. D. Sun's research group to study "Propagation characteristics of binary grating-graphene layer structures in terahertz range" after returning to the Harbin Institute of Technology. Pengzi earned her Bachelor of Science degree in July, 2013. A month later she joined the Master of Science program in Applied Physics at Cornell University.

Pengzi's Master thesis, entitled "Thickness and Stacking Sequence Determination of 1T-TaS_2 Using Scanning Transmission Electron Microscopy" was supervised by Dr. Lena F. Kourkoutis.

I would like to dedicate this thesis to my family, my friends and my supervisor, Professor Lena Fitting Kourkoutis.

ACKNOWLEDGMENTS

I would like to express my gratitude to all those who helped me during the writing of this thesis.

First and foremost, my deepest gratitude goes to my advisor Prof. Lena F. Kourkoutis for her consistent and illuminating guidance. She led me into the amazing field of electron microscopy and kept helping me in all aspects of my study. Without her patient instruction and warm encouragement, the completion of thesis would not have been possible. Also I would like to thank Prof. Darrel Schlom for serving on my special committee.

Secondly, I am most grateful to Dr. Robert Hovden, Prof. David A. Muller, and Dr. Earl J. Kirkland for their invaluable discussions and advice on the topic of my thesis.

I would also like to thank all members of the Kourkoutis Electron Microscopy group. Special thanks to David Baek for his guidance on sample preparation and microscopy in academic level, and being such a good friend in personal level. I would like to mention Xue Bai, Jade Noble, Benjamin Savitzky, Katherine Spoth, Michael Zachman, Mallika Bariya and Suk Hyun Sung for making my life so joyful at Ithaca.

I am grateful to all my dear friends for their support and patience all the time. Special thanks to Yimo Han for her companionship, and Zhongyi Zhang for his technical support.

Additionally, I also thank the School of Applied and Engineering Physics for their support and assistance through the two-year program.

Last but certainly not least, my gratitude also extends to my beloved family who have been supporting me with their unconditional love since I came to this wonderful world.

Without their loving considerations and great confidence in me I would not have so much freedom to chase my dream of pursuing knowledge and truth.

TABLE OF CONTENTS

LIST OF FIGURES

LIST OF TABLES

CHAPTER 1

INTRODUCTION & MOTIVATION

Beyond graphene, the interest in exploring characteristics of other two-dimensional (2D) materials has intensified over the last decade. Interestingly, atomically thin films of 2D transition metal dichalcogenides (TMDs) exhibit layer-dependently electronic properties that significantly differ from properties in bulk crystals. For example, MoS_2 has an indirect bandgap of 1.23eV in bulk [1], while a direct bandgap of 1.9 eV is observed for a single-layer (SL), which gives rise to a strong enhancement in luminescence compared to bulk [2,3]. By theoretical predictions [4], electronic band structures and absorption spectra of bilayer (BL) TMDs including MoS_2, $MoSe_2$, WS_2, and WSe_2 can also be modified by changes in the stacking sequence. Although challenging, the stacking sequence-dependent tuning of bandgaps is promising in applications of electromechanical devices, tunable photodetectors, and lasers [4]. For the more metallic-like TMD 1T-TaS_2, a rich set of phenomena emerges at low temperature, including metal-insulator transitions and even superconductivity of high pressures or upon dopings [5-7]. Research in this field was also stimulated by realizing the electronic control of exotic charge-density-wave (CDW) phase transitions in 1T-TaS_2. By thinning down from bulk crystals, recent efforts achieved thickness-dependent manipulation of CDW phases within atomically layered 1T-TaS_2-based ionic field-effect transistor [8], which provided pathways to understand the physics of CDW phase transitions. However, limited work focused on exploring the influence of the stacking sequence of the layered 1T-TaS_2 thin film on the CDW phase transitions.

With the aberration corrected scanning transmission electron microscopy (STEM), we imaged the grain boundary in layered 1T-TaS_2 sheets at atomic-resolution when viewed along c-axis (planar vector). As shown in Figure 1.1, bright atoms represent Ta in these high-angle annular dark-field (HAADF) STEM images. Interestingly, a structural transition from the left region with typical trigonal structure to the right region with a hexagonal structure within approximately 50Å was observed in the HAADF-STEM image. Meanwhile, Fourier transforms revealed the existence of CDW peaks in reciprocal space for both regions. Hence, our research is motivated by filling the knowledge gap between changes in thickness and stacking sequence for layered structures of 1T-TaS_2 and the development of CDWs. Thus, in this work, our focus is to understand the dramatic change of contrast recorded in experimental images by extracting both thicknesses and stacking sequences of layered 1T-TaS_2 thin flakes.

As reported in previous work [9-12], convergent-beam electron diffraction (CBED) is a reliable technique to determine the thickness and symmetry of a wide range of materials. Formed by a focused electron probe that is incident on the sample, CBED patterns consist of diffraction disks of different orders and are highly sensitive to sample thickness and symmetries. By combining experiment and simulation, CBED patterns can be used to determine sample thickness and symmetries. Hence, the analysis of CBED patterns acquired from both experiment and simulations is the key point of our research.

In Chapter 2, I will cover the layered structure and stacking sequence of 1T-TaS_2. The science of HAADF-STEM images and CBED patterns obtained by both experiment

and simulation techniques will also be discussed in Chapter 2. I will demonstrate our process to determine thicknesses and stacking sequences of 1T-TaS_2 layered structures by comparing experimental and simulated results in Chapter 3. The final outcomes and limitations of our method will be discussed in Chapter 4. In Chapter 5, I will summarize our research and talk about our future work.

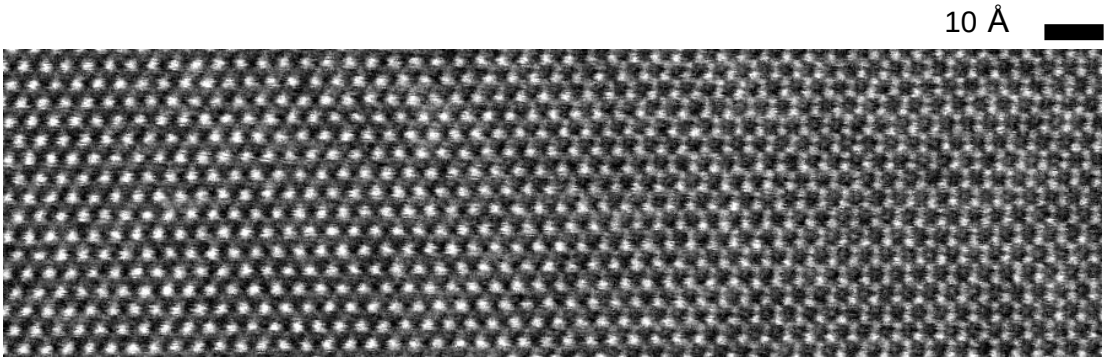

Figure 1.1: HAADF-STEM image (taken by Robert Hovden) showing a domain boundary of layered 1T-TaS_2 sheets at atomic-resolution along [001].

CHAPTER 2

THEORETICAL BACKGROUND

2.1 Layered Structures and Stacking Sequences of 1T-TaS_2

In general, TMD crystals adopt a layered structures with different stacking arrangements of X-M-X sandwiches (Figure 2.1(a)), where M is a transition metal atom (Mo, Ta, W, etc.) and X is a chalcogen atom (S, Se, etc.) [13]. At the same time, various polytypes of bulk TMD crystals exist due to variations of the three-atom-thick sandwich structure. As shown in Figure 2.1(b), the metal atom is in an octahedral geometry for the 1T (trigonal) modification, while for the 2H (hexagonal) phase, the Ta atoms are coordinated in a trigonal-prismatic fashion.

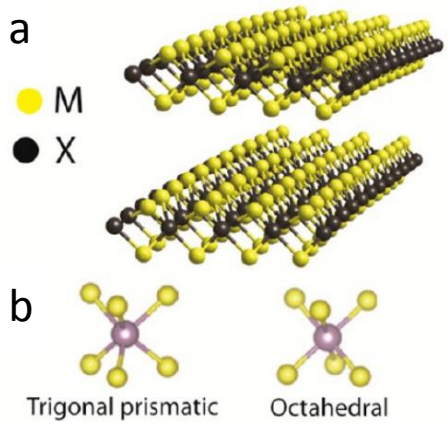

Figure 2.1: Layered structure of TMD crystals. (a) M-X-M sandwich structure. (b) Trigonal prismatic and octahedral polytypes of TMD crystal [13].

2.1.1 Layered structure of 1T-TaS_2

The structure of both single-layer and bulk crystal 1T-TaS_2 are demonstrated in Figure 2.2. As displayed in Figure 2.2(a), the S-Ta-S structure in single-layer 1T-TaS_2 has an octahedral polytype, showing that each Ta atom is surrounded by six nearest neighbor S atoms. Alternatively, when examined in the (001) projection plane (Figure 2.2(b)), the hexagonal lattice can be found with each Ta atom surrounded by six nearest neighbor Ta atoms. Along the [001] orientation (c-axis) of crystalline 1T-TaS_2, Ta atoms lie atop of each other while S atoms do not overlap in one unit cell (Figure 2.2(c)).

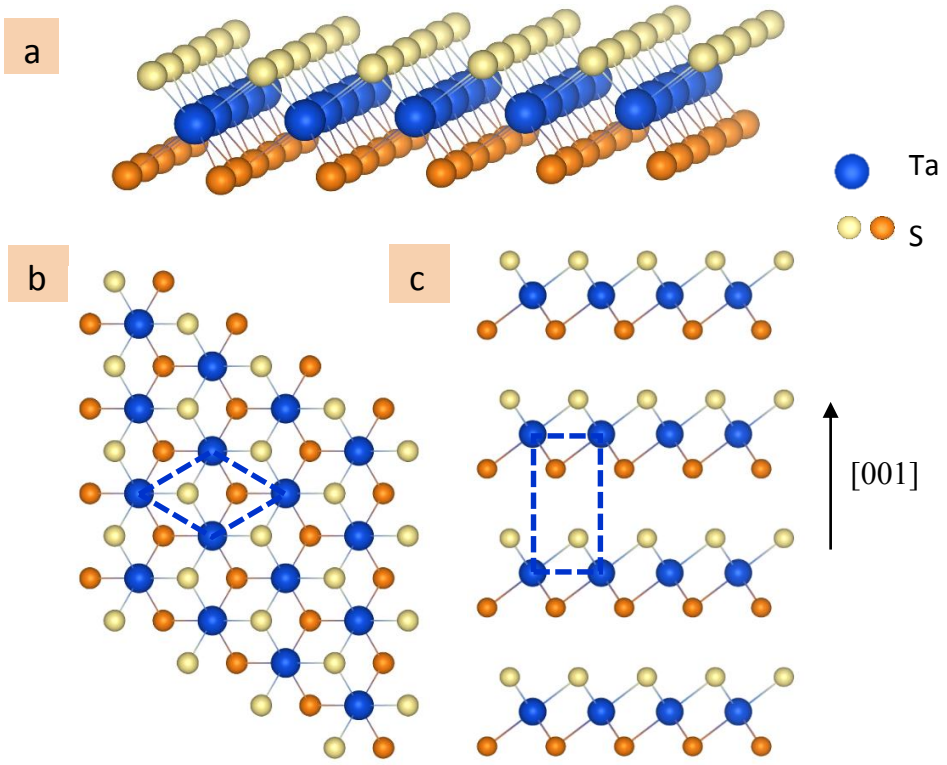

Figure 2.2: Structures of Single-layer and bulk 1T-TaS_2. (a) Single-layer, (b) plan-view and (c) side-view of 1T-TaS_2.

2.1.2 Stacking sequences of 1T-TaS_2

The layered nature of 1T-TaS_2 is a result of weak interlayer van der Waals forces [14], which not only facilitates the isolation of 1T-TaS_2 thin films by mechanical [8, 15] exfoliation, but also provides the possibility of shifting between atomic layers. Figure 2.3(c) gives an illustration of the shifting that gives rise to a transition in image contrast from a trigonal structure (Figure 2.3(a)) to a hexagonal structure (Figure 2.3(b)). Here, the illustration suggests that all Ta sites in some layers shift a bond length relative to the other layers. Since in HAADF-STEM images ("Z-contrast" images) heavier atoms contribute more to the intensity than lighter atoms, the image contrast is dominated by the heavy Ta atoms. The structural transition between domains in the thin 1T-TaS_2 flake (Figure 2.3(d)) is therefore clearly visible. Our goal is to study the structural change between layers in the direction perpendicular to the imaging plane, i.e. to explore stacking sequences of the layered structure of 1T-TaS_2 in a quatitative manner.

2.2 Charge density waves of 1T-TaS_2

Upon cooling, bulk 1T-TaS_2 undergoes a series of charge density wave (CDW) phase transitions which are coupled to both electron transport properties and lattice structure. Transition temperatures for the metallic incommensurate CDW (ICCDW), the nearly commensurate CDW (NCCDW) phase, and commensurate CDW (CCDW) phase are 355 K and 225 K, respectively [5-7]. With a push towards ultrathin 1T-TaS_2 films, recent research [8, 16-18] reported that both transition temperatures could be strongly modulated by the thickness of 1T-TaS_2 (Figure 2.4(a)). As shown in Figure 2.4(b), both

transition temperatures decrease as the sample thickness is reduced. Interestingly, ICCDW/NCCDW and NCCDW/CCDW transitions disappear at critical thicknesses of ~ 3 nm (5 layers) and ~10 nm (17 layers), respectively.

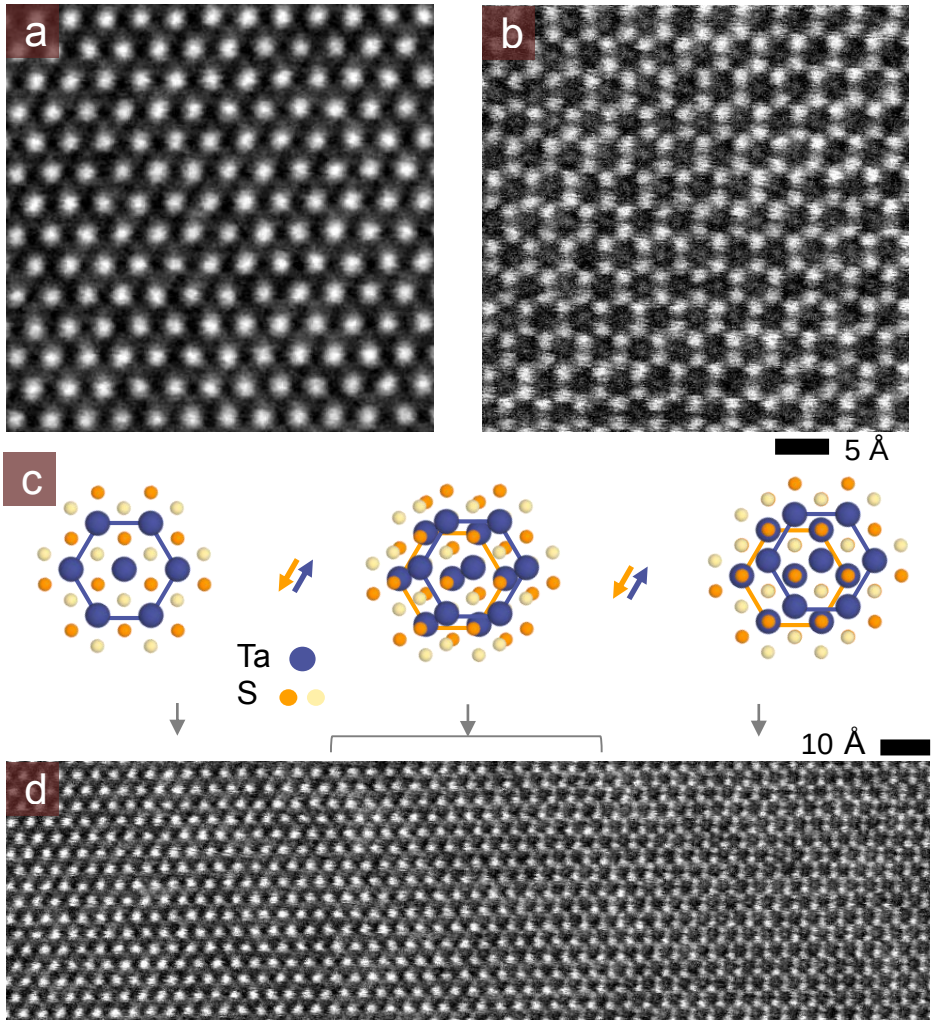

Figure 2.3: HAADF-STEM image showing the domain boundary of layered 1T-TaS_2 sheets at atomic-resolution along [001]. (a) and (b) are magnified images of trigonal and hexagonal structures observed in (d). (c) Illustration of the layer shifting that results in a transition in image contrast from a (a) trigonal structure to a (b) hexagonal structure. Images recorded by R. Hovden.

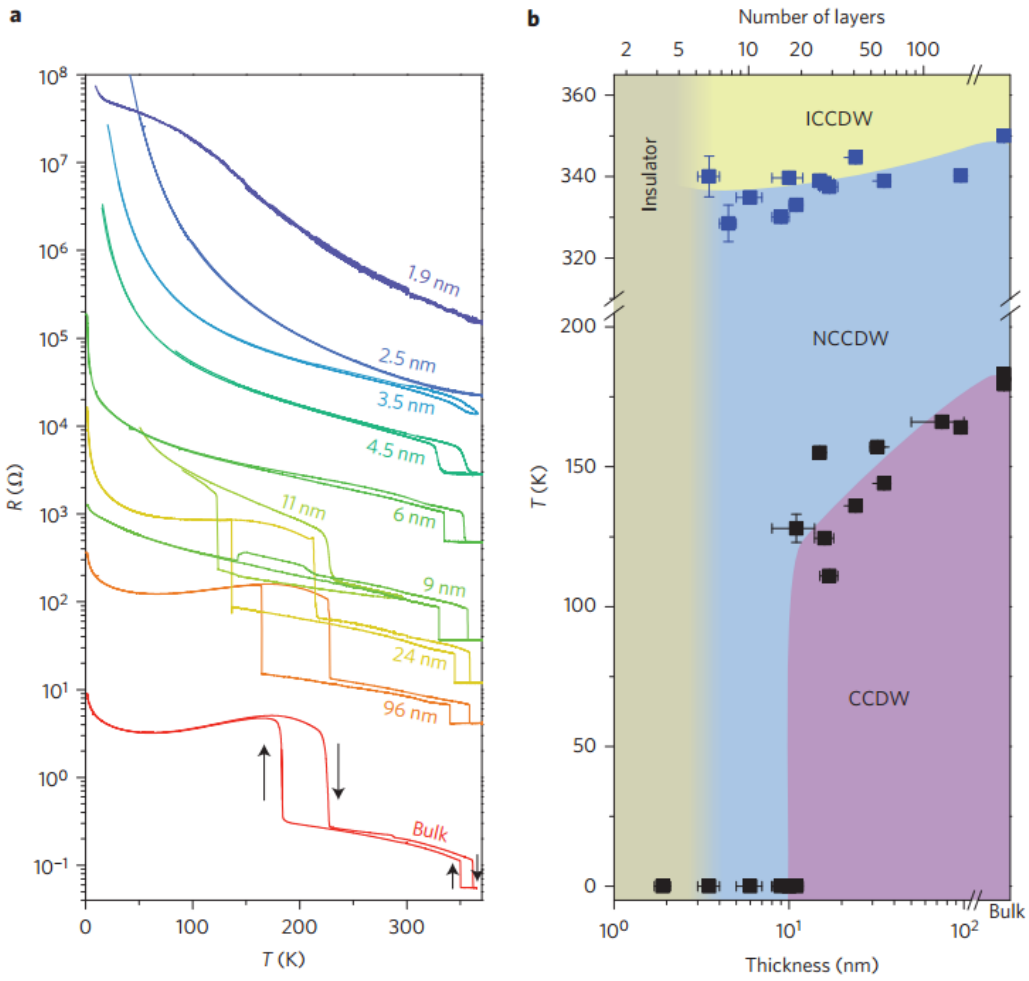

Figure 2.4: CDW phases in 1T-TaS2 thin flakes at different thicknesses. (a) Resistance as a function of temperature for 1T-TaS2 thin flakes at varying thicknesses. (b) Thickness-temperature phase diagram showing phase boundaries [8].

2.3 Experimental techniques

2.3.1 Annular-dark field scanning transmission electron microscopy

In scanning transmission electron microscopy (STEM) a focused small electron probe (typically 1 to 2 Å) is scanned across the sample and scattered electrons are collected by an annular-dark-field (ADF) detector to produce a two-dimensional projection image

(Figure 2.5). Since the contrast in HAADF-STEM images is strongly dependent on atomic number Z, heavier atoms appear to be brighter compared with lighter atoms.

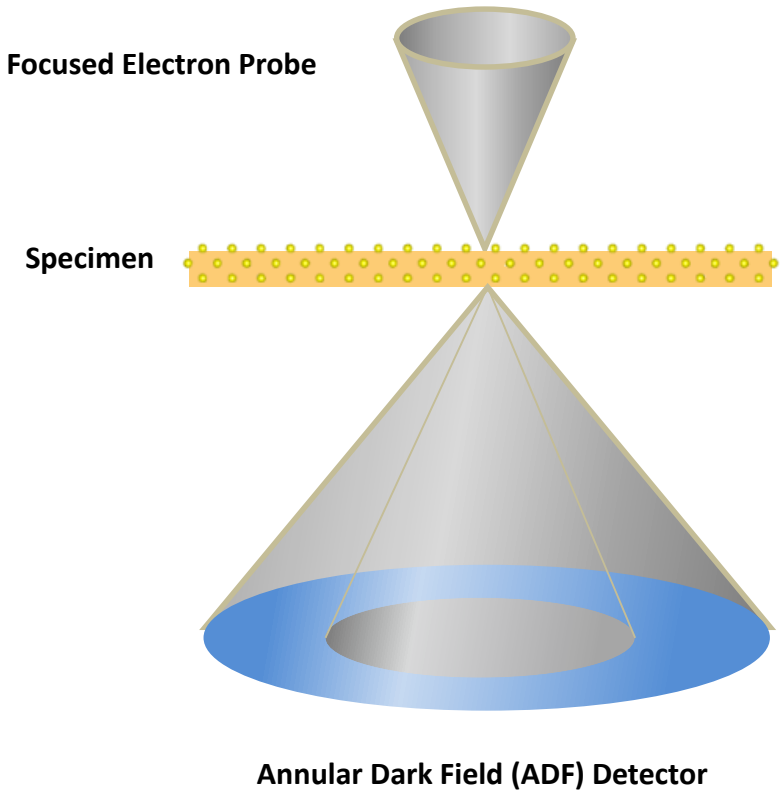

Figure 2.5: Schematic of ADF-STEM imaging process.

2.3.2 Aberration-corrected STEM

The main limitations of resolution in STEM can be roughly divided into geometric aberrations and chromatic aberrations. Geometric aberrations are usually introduced by the imperfectness of magnetic lenses and the aberration function can be written as [19]:

$$\chi(\alpha) = \frac{2\pi}{\lambda}\left(-\frac{1}{2}\,\Delta f\,\alpha^2 + \frac{1}{4}\,C_3\,\alpha^4 + \frac{1}{6}\,C_5\,\alpha^6 + \frac{1}{8}\,C_5\,\alpha^8 + \cdots\right), \qquad (2.1)$$

where α is the convergence semi-angle and $\chi(\alpha)$ is the phase shift with a tolerance of $\pi/2$. Here we don't show the full derivation the optimal convergence angle and probe size. With given aberrations at the beam energy, we can calculate the maximum convergence angle and corresponded probe size.

Figure 2.3(a,b,d) are taken with third and fifth-order aberration-corrected NION UltraSTEM operating at 60keV. Since resolution in such system is mainly limited by chromatic aberrations, and the optimal aperture size and probe size are given by $\alpha_{\max} = 1.2\,(\frac{\lambda E_0}{C_C\,\delta E})^{1/2}$ and $d_{\min} = 0.52\,(\frac{\lambda C_C\,\delta E}{E_0})^{1/2}$, respectively [20]. Since the chromatic aberration coefficient $C_C = 1.3$ mm, and the energy spread $\delta E = 0.35$eV, if we ignore effects of the relativity, then the optimal aperture size and probe size are $\alpha_{\max} = 30.8$ mrad and $d_{\min} = 1.0$ Å. Hence we could obtain HAADF-STEM images with aberration-corrected NION UltraSTEM at atomic resolution as shown in Figure 2.3(a,b,d).

2.3.3 Convergent-beam electron diffraction

Convergent-beam electron diffraction (CBED), as a major technique in modern electron microscopy, offers an effective pathway to three-dimensional (3D) crystallographic analysis for a wealth of materials. By controlling the shape of the incident electron beam, e.g. parallel or convergent illumination, different diffraction modes can be achieved. The comparison between conventional selected-area electron diffraction (SAED) and CBED is schematically illustrated in Figure 2.6. For SAED, the selected region of the specimen is illuminated by a parallel electron beam. A selected-area

aperture on the beam path will block irrelevant sections of all beams transmitted through the specimen, so that only diffracted beams of interest will be examined and form projection patterns of the reciprocal lattice as orders of diffraction spots. An illustration of the SAED pattern for crystalline Si is depicted in (100) direction (bottom left).

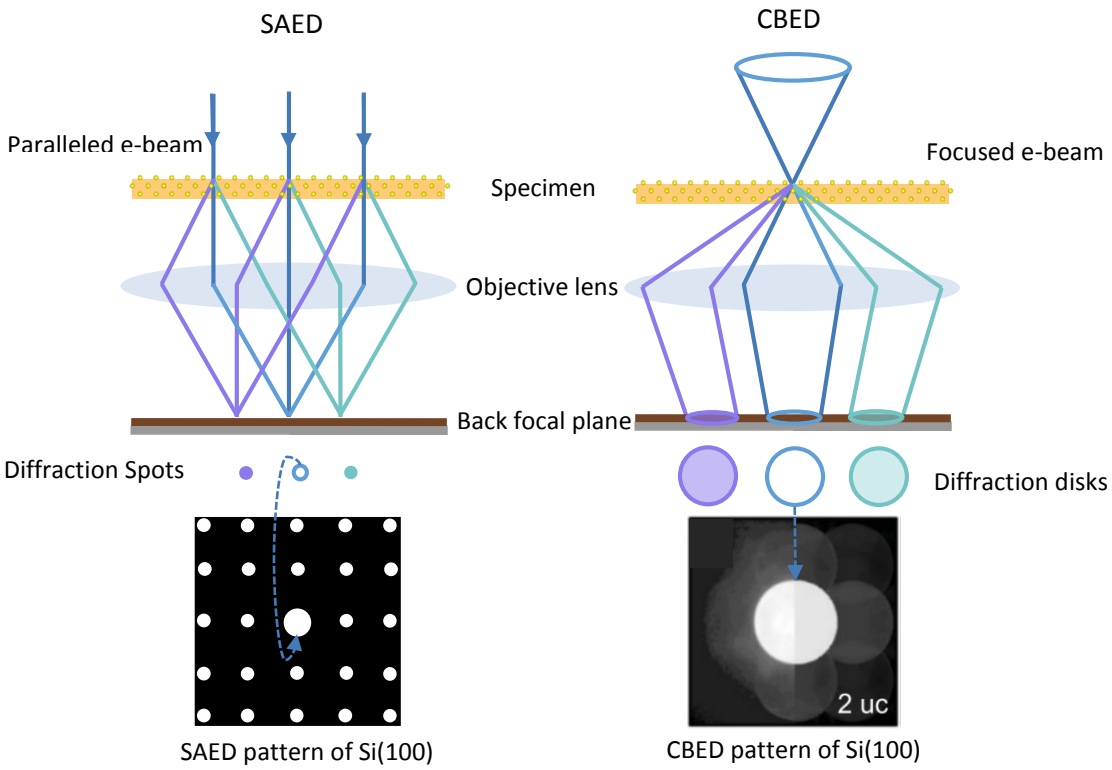

Figure 2.6: Schematics of obtaining SAED and CBED patterns.

The most essential difference between SAED and CBED is the shape of incident beam. In STEM, the electron beam is focused by the system of condenser lenses and the pre-field of the objective lens. As shown in Figure 2.6 (right), the sub-nanoscale (usually 1-2Å) focused probe is parked and incident on the specimen. After passing through the illuminated region, transmitted electrons will form a set of divergent cones and their cross-sections will enlarge as these cones travel in the STEM column. Therefore, instead

of a series of diffraction spots, there will be diffraction disks containing rich details of contrast and patterns rather than the uniform intensity.

If the probe size is smaller than a unit cell, and the electron probe is scanned while taking the CBED pattern, the final pattern will be an incoherent average of many CBED patterns acquired at different positions in the whole scanned area [21]. This technique, called position-averaged CBED (PACBED), has been applied for thickness determination of various materials [9-12].

2.4 Multislice simulations

2.4.1 The weak phase object approximation and atomic potentials

The weak phase object (WPO) approximation [22] suggests that the imaging electrons transmit through a thin specimen with a decrease in wavelength, and the depletion can be treated equivalent as a small phase shifting θ:

$$\theta = \sigma v_z(\mathbf{x}) , \tag{2.2}$$

where interaction parameter σ is:

$$\sigma = \frac{2\pi\lambda me}{h^2} , \tag{2.3}$$

and m is the relativistic mass. The projected atomic potential $v_z(\mathbf{x})$ is calculated as:

$$v_z(\mathbf{x}) = v_z(x,y) = \int_0^t v_s(x,y,z)\,\mathrm{d}z , \tag{2.4}$$

where $v_s(x, y, z)$ is the atomic potential at each thickness z.

The interaction parameter is ~ 0.7 radians/(kV•Å) at a beam energy of 200 keV, and the projected atomic potential of Au (Z=79) is 1.45 kV•Å at a radius of 0.1 Å [23], thus a single gold atom can produce a phase shift of ~ 1.0 radians, which is not weak. Although the projected atomic potential of Ta (Z=73) is smaller than gold, in the strict framework of the WPO approximation, Ta shouldn't be treated as a WPO.

2.4.2 Multislice simulations for ADF-STEM images and CBED patterns

In our work, ADF-STEM images and CBED patterns were simulated using the multilice method illustrated in Figure 2.7. The specimen is divided into *n* thin slices with thickness Δz, and the projected atomic potential in each slice will cause a small phase shift of the wavefunction for incident electrons. Between slices electrons propagate a distance of Δz with Fresnel diffraction. After transmitting through the whole specimen, the exit wavefunction is diffracted onto the ADF detector plane, and the square of transmitted wave function is the CBED pattern corresponding to the probe position. If incoherently integrating the CBED pattern over the detector geometry then the final result is the ADF-STEM intensity at the probe position. Next the multislice program will repeat the same process for another probe position in the desired region until the final ADF image is generated.

If the wavefunction of the probe focused at a specific position $\mathbf{x}_p$ of the first slice (surface of the specimen) is described as $\psi_p(x, y, z, \mathbf{x}_p)$, then the transmitted wavefuction after passing through the first slice is:

$$\psi_1(x, y, z + \Delta z, \mathbf{x}_p) = p(x, y, \Delta z) \otimes \left[t_1(x, y, z)\psi_p(x, y, z, \mathbf{x}_p)\right] + O(\Delta z^2), \quad (2.5)$$

where $\otimes$ represents convolution, $t_1(x, y, z)$ is the transmission function:

$$t_1(x, y, z) = \exp\left[i\sigma \int_{z_1}^{z_1+\Delta z} v_1(x, y, z')dz'\right], \quad (2.6)$$

and $p(x, y, \Delta z)$ is the propagation function:

$$p(x, y, \Delta z) = \frac{1}{i\lambda\Delta z} \exp\left[\frac{1}{i\lambda\Delta z}(x^2 + y^2)\right], \quad (2.7)$$

thus, after exiting the last slice labeled with *n* the electron wavefunction can be described as:

$$\psi_n(x, y, \mathbf{x}_p) = p(x, y, \Delta z) \otimes \left[t_n(x, y, z)\psi_{n-1}(x, y, z, \mathbf{x}_p)\right] + O(\Delta z^2), \quad (2.8)$$

then the CBED pattern can be calculated as:

$$\left|\Psi_n(k_x, k_y, \mathbf{x}_p)\right|^2 = \left|FT[\psi_n(x, y, \mathbf{x}_p)]\right|^2, \quad (2.9)$$

and the ADF intensity is:

$$I(\mathbf{x}_p) = \int \left|\Psi_n(k_x, k_y, \mathbf{x}_p)\right|^2 G(\boldsymbol{k}) d^2\boldsymbol{k}, \quad (2.10)$$

where $G(k)$ is the detector function in the ADF-STEM mode:

$$G(\boldsymbol{k}) = \begin{cases} 1, & k_{inner} \leq k \leq k_{outer} \\ 0, & otherwise \end{cases} . \tag{2.11}$$

Therefore the CBED pattern and ADF-STEM intensity at a specific probe position are produced. The final image of desired region is simulated by repeating the same process for each position of the focused probe [23].

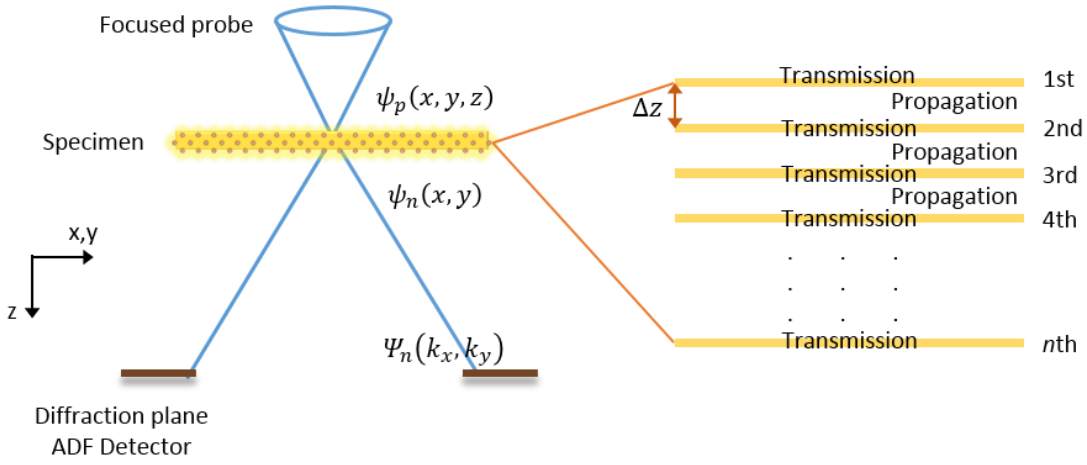

Figure 2.7: Schematic of the multislice method.

CHAPTER 3

METHODS

3.1 Configurations of 1T-TaS_2 stacking sequence

3.1.1 Stacking sequences of bilayer 1T-TaS_2

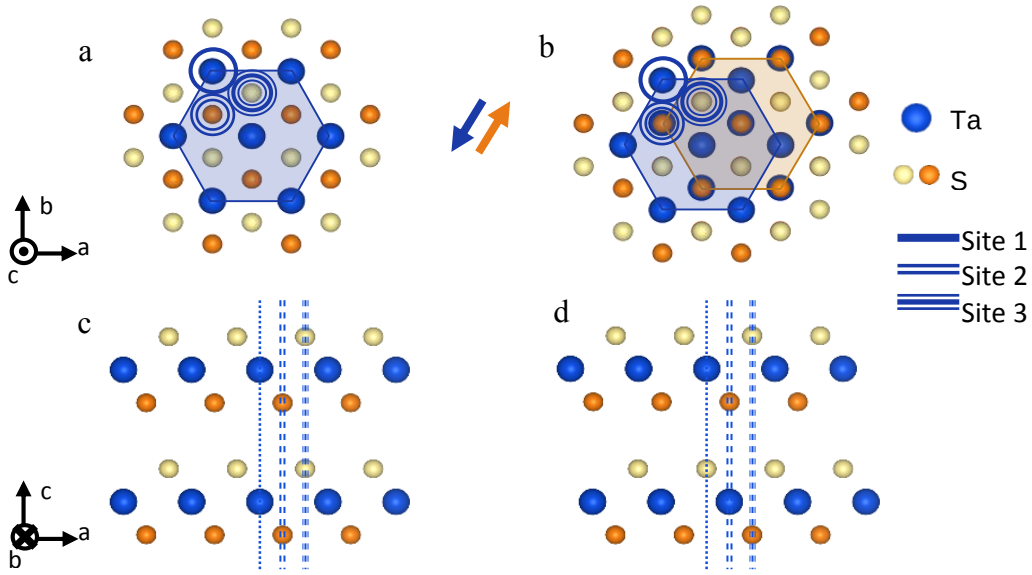

Figure 3.1: Stacking sequences of BL 1T-TaS_2. (a) Plan-view and (c) side-view of AA stacking. (b) Plan-view and (d) side-view of AB stacking.

As discussed in Chapter 2, we observed a transition in the arrangement of Ta sites from a trigonal structure to a hexagonal structure. An illustration of different stacking sequences of layered 1T-TaS_2 was used to explain the structural transition by presenting. Starting with the simplest case, Figure 3.1(a) displays a top view of typical trigonal stacking of bilayer (BL) 1T-TaS_2. In an alternative representation (Figure 3.1(b)) it is clearly shown that all Ta atoms are aligned along the c-axis (zone-axis in HADDF-STEM images). Meanwhile, only the atomic column of Site 1 (labeled by the single-

solid line) is taken by Ta atoms among all three different sites in one unit cell. However, if all Ta sites in the top layer shift a bond length relative to the bottom layer (Figure 3.1(c) and (d)), then atomic columns of both Site 1 and Site 2 (circled by the double-solid line) will be occupied by Ta atoms, which creates the other stacking sequence of bilayer 1T-TaS_2. Therefore, the top view of such stacking reveals a hexagonal rather than a trigonal structure of Ta sites (Figure 3.1(c) and (d)).

To distinguish these two stacking sequences and facilitate later discussions, I will use the convention as listed in Table 3.1. A single layer is named "A" with Site 1, Site 2 and Site 3 (labeled in Figure 3.1) taken by Ta, S and S atoms respectively; while layer "B" indicates that three sites are taken by S, Ta and S atoms sequentially in a single layer, and layer "C" is defined as a single layer 1T-TaS_2 sheet with S, S and Ta atoms on three sites sequentially.

Table 3.1: All configuration of stacking sequences for BL 1T-TaS_2.

	AA		AB		AC		BA		BB	
	Top layer	Bottom layer	Top layer	Bottom layer	Top layer	Bottom layer	Top layer	Bottom layer	Top layer	Bottom layer
Site 1	Ta	Ta	Ta	S	Ta	S	S	Ta	S	S
Site 2	S	S	S	Ta	S	S	Ta	S	Ta	Ta
Site 3	S	S	S	S	S	Ta	S	S	S	S

	BC		CA		CB		CC	
	Top layer	Bottom layer	Top layer	Bottom layer	Top layer	Bottom layer	Top layer	Bottom layer
Site 1	S	S	S	Ta	S	S	S	S
Site 2	Ta	S	S	S	S	Ta	S	S
Site 3	S	Ta	Ta	S	Ta	S	Ta	Ta

In fact, here we ignored the difference between coordinates in c-axis of two sulfur atoms. If Layer A is turned upside down then a different structure labelled as Layer A' will be obtained (Figure 3.2). Layer B' and Layer C' can be defined by the similar process. Thus, there exist 6^2 different stacking sequences for BL 1T-TaS_2 mathematically. However, if we use the linear imaging model for thin specimens illustrated in Chapter 2, then the effect of absolute coordinates of sulfur atoms along the optic axis can be overlooked, which eliminates the difference between Layer A and Layer A'.

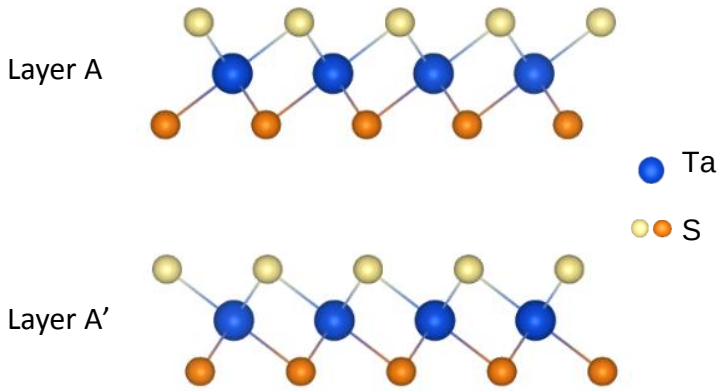

Figure 3.2: Illustrations of Layer A and Layer A'.

3.1.2 Symmetries of stacking sequences for 1T-TaS_2 in the projection plane

We deduced nine (3^2) different stacking sequences for BL 1T-TaS_2 (Table 3.1). Since there are 3^n possible configurations of stacking for n-layer 1T-TaS_2, it is necessary to reduce these configurations in terms of further study.

Again, if we use the linear imaging model of ADF projected intensity described in Chapter 2, then the effect of absolute coordinates of Ta and S atoms along the optic axis

can be ignored based on two assumptions. On the one hand, a Ta atom lying atop of a sulfur atom can be treated as the same case when their positions are reversed, so that BA, CA and CB stacking equal to AB, AC and BC stacking respectively. On the other hand, variations of the distance between Ta atoms and S atoms along atomic columns can be neglected. Hence, in combination with a rotation of 60^{o} along appropriate axes perpendicular to the projection plane, the lack of variation will equal AB and AC stacking (Figure 3.3). At the same time, note that AA/BB/CC stacking can be treated as the same structure from the perspective of rotational symmetry. BC/CA stacking can be obtained by rotating AB stacking with 120^{o} along appropriate axes perpendicular to the projection plane.

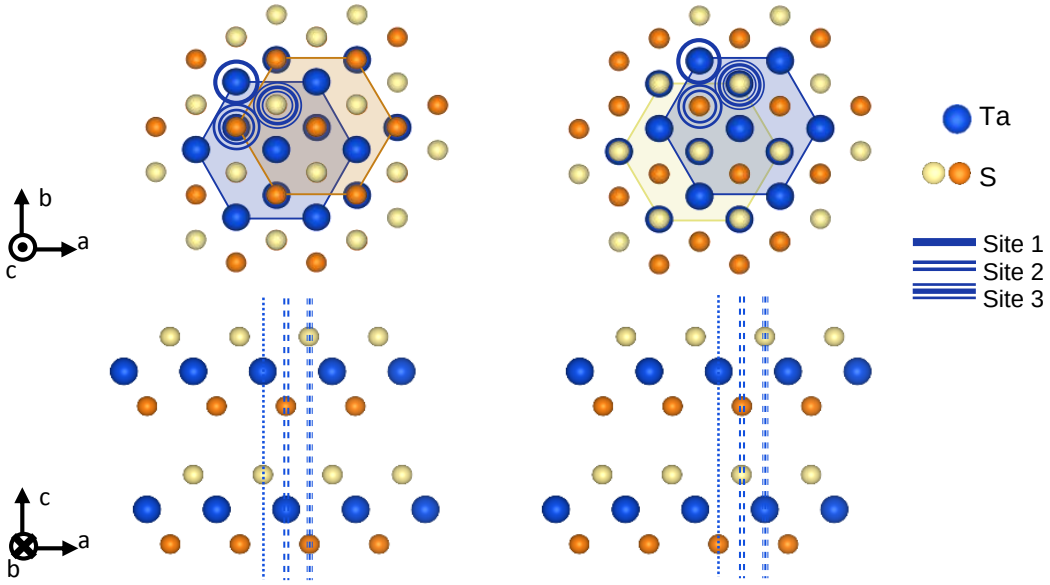

Figure 3.3: Illustrations of AB (left) and AC (right) stacking.

Therefore, for BL 1T-TaS_2, we will only consider two possible stacking sequences: either AA or AB stacking. Similarly, we can simplify stacking configurations for multi-layer 1T-TaS_2 using these two assumptions.

3.1.3 Configurations of stacking sequences for multi-layer 1T-TaS_2

By adding another layer to BL 1T-TaS_2, there will be three different configurations (Table 3.1): AAA, AAB and ABC stacking (Figure 3.4). Obviously, AAA and AAB stacking can be treated as adding another layer right atop of BL 1T-TaS_2. While in ABC stacking, there is a bond-length shift between each two layers, so that Ta atoms exist in all three sites (columns), which makes Ta sites a trigonal structure in the (001) projection plane.

For 1T-TaS_2 with more (>4) layers, more configurations will appear and we will discuss the influence of different stacking sequences on both experimental and simulated HAADF-STEM images in Chapter 4. Note that the most bulk-like stacking configuration is AA…AA stacking, i.e. all-A stacking, therefore it's very convenient to take all-A stacking as a good starting point of simulation. All stacking configurations for 1T-TaS_2 with three to ten layers will be listed in the Appendix.

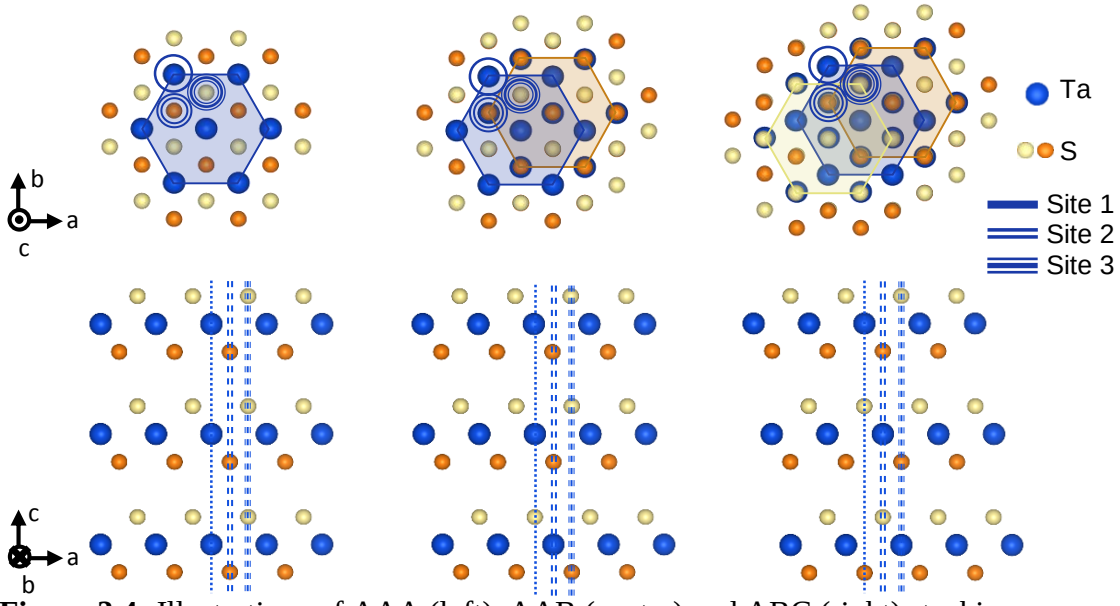

Figure 3.4: Illustrations of AAA (left), AAB (center) and ABC (right) stacking.

3.2 Interpretation of 1T-TaS_2 structure

For image simulations, it is very important to translate the structure of materials into input files that can be recognized by simulation programs. In multislice simulations, a full *.xyz* input file is in the format shown in Table 3.2.

Table 3.2 The format of the input data for *incostem.m* and *autostem.m* [23]

<comment line>
ax by cz
Zatom1 xpos1 ypos1 zpos1 occ1 wobble1
Zatom2 xpos2 ypos2 zpos2 occ2 wobble2
: : : :
ZatomN xposN yposN zposN occN wobbleN
-1

The first line (comment line) is ignored by *incostem.m* and *autostem.m* programs, and the second line describes the three dimensional size of one unit cell (in Angstroms). Starting from the third line are the atomic numbers, coordinates, occupancies, and random displacements caused by thermal vibrations for each atom in one unit cell. The input file is ended with -1 as required by programs.

3.2.1 The rectangular unit cell and lattice constants of 1T-TaS_2

The basic structure of 1T-TaS_2 with a trigonal lattice in space group ($P\bar{3}m1$) with $a = b \neq c$, $\alpha = 60^o$ and $\beta = \gamma = 90^o$ is shown in Figure 3.5. The primitive unit cell consists of

one Ta atom at (0, 0, 0) and two S atoms at (1/3, 1/3, 1/4) and (2/3, 2/3, 3/4), respectively [24].

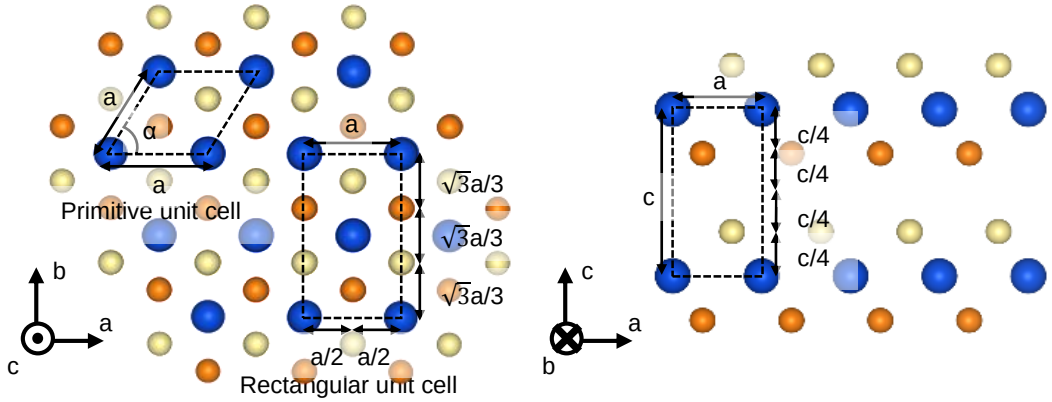

Figure 3.5: Illustrations of rectangular unit cell of 1T-TaS_2.

Since it is more convenient to describe the specimen with rectangular unit cells than typical primitive cells for multislice simulations, we need to interpret the structure of 1T-TaS_2 as a rectangular unit cell with $b = \sqrt{3}a$ in Figure 3.5. In our work, lattice parameters of a = 3.36 Å, $b = \sqrt{3}a$ = 5.82 Å, and c = 5.90 Å [25] are applied to simulations.

3.2.2 Thermal vibrations and Debye-Waller factors

So far we obtained the ideal positions of atoms in 1T-TaS_2, however instead of being stationary in a certain position, every atom vibrates with small displacements (usually 10^{-2}Å) at some frequencies, and these atomic vibrations are quantized as phonons. Typically, phonons in optical modes have frequencies at 10^{12} to 10^{13} Hz while acoustic phonons have much lower frequencies [26]. And the travel time for electron in the specimen at a thickness around 10 nm is only ~ 10^{-16} s. Therefore atoms can be treated

as being frozen while imaging electrons pass through the specimen. Meanwhile, considering the time interval between successive imaging electrons is much longer than periods of phonons [23], electrons actually interact with the same atoms in different locations or phonon modes. Thus, for more accurate simulation results we need to take different phonon configurations into account with frozen phonons [27,28]. In frozen phonon approximation, offsets (in three dimensions) of each atom is randomly generated by the Gaussian distribution with a mean value of the original coordinate and a standard deviation of the root-mean-square displacement referred to each atom (known as Debye-Waller factor). Note that the atomic offsets are fixed in each phonon configuration but independent for different phonon configurations. And the intensity of final images is produced by incoherently averaging images calculated with each phonon configurations.

In our work, the Debye-Waller factor of 0.0927 Å [29] is applied for both Ta and S atoms in a convenient approach. For more accurate calculations, different Debye Waller factors should be used for Ta and S atoms, respectively.

3.3 Incoherent image simulations of 1T-TaS_2

The incoherent image simulation in the set of multislice programs by Kirkland can be interpreted as a linear convolution of the probe wavefunction with the atomic potentials, thus, the final image is a pure mass mapping of the projection plane (see detailed discussion in the Appendix). Results from incoherent linear imaging calculations cannot be used for strict quantitative analyses, but are very useful for quickly checking the

correctness of input parameters, especially the coordinates of structures. As shown in Figure 3.6, ADF-STEM images were calculated by the incoherent imaging model with different stacking sequences of BL 1T-TaS_2. Figure 3.6 illustrates the typical trigonal lattice and the hexagonal structure of AA stacking and AB stacking, respectively. An aperture semi-angle of 26 mrad, a beam energy of 60keV, and detector angles ranging from 80 mrad to 240 mrad were chosen. Each image represents an area of 3×2 uc^2 (10.08×11.64 $Å^2$) in real space.

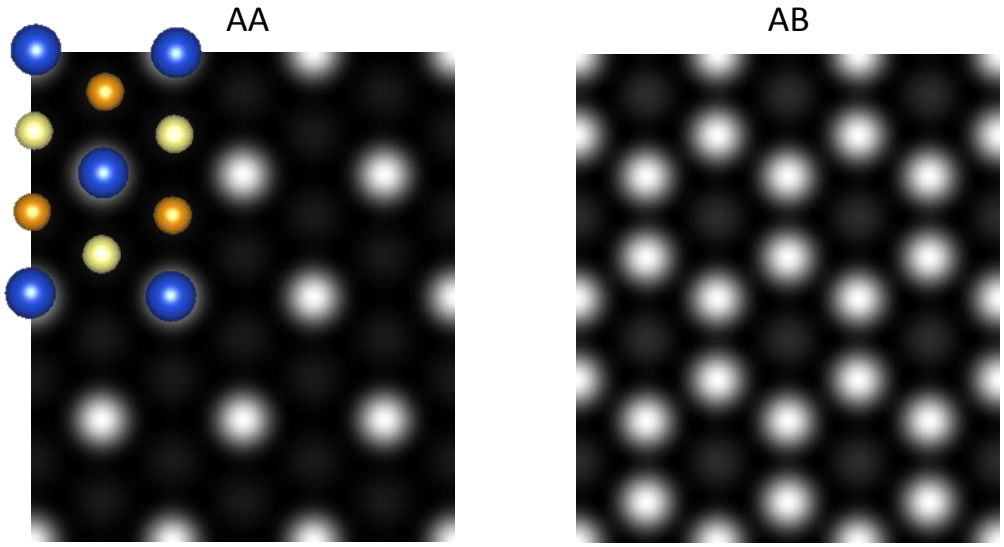

Figure 3.6: Incoherent simulations with the linear imaging model of HAADF-STEM images of 1T-TaS_2 with AA stacking and AB stacking.

3.4 Multislice simulations for extracting the thickness and stacking sequence of 1T-TaS_2

Using the multislice approach previously discussed in Chapter 2, we simulated ADF-STEM images and CBED patterns for different thicknesses and stacking sequences of 1T-TaS_2. By analyzing simulated results, we are able to study the influence of the

stacking sequence and thickness on HAADF-STEM image contrast and extract structural information along 1T-TaS_2 [001].

3.4.1 HAADF-STEM images

Figure 3.7(a) shows Moiré patterns in the HAADF-STEM image of layered 1T-TaS_2 on [001] zone-axis. At larger magnification, Ta atoms are more visible as bright spots in region A and region B, and Ta sites exhibit two different structures as shown in Figure 3.7(b,c). Meanwhile, region A (hexagonal) has a higher intensity compared with region B (trigonal).

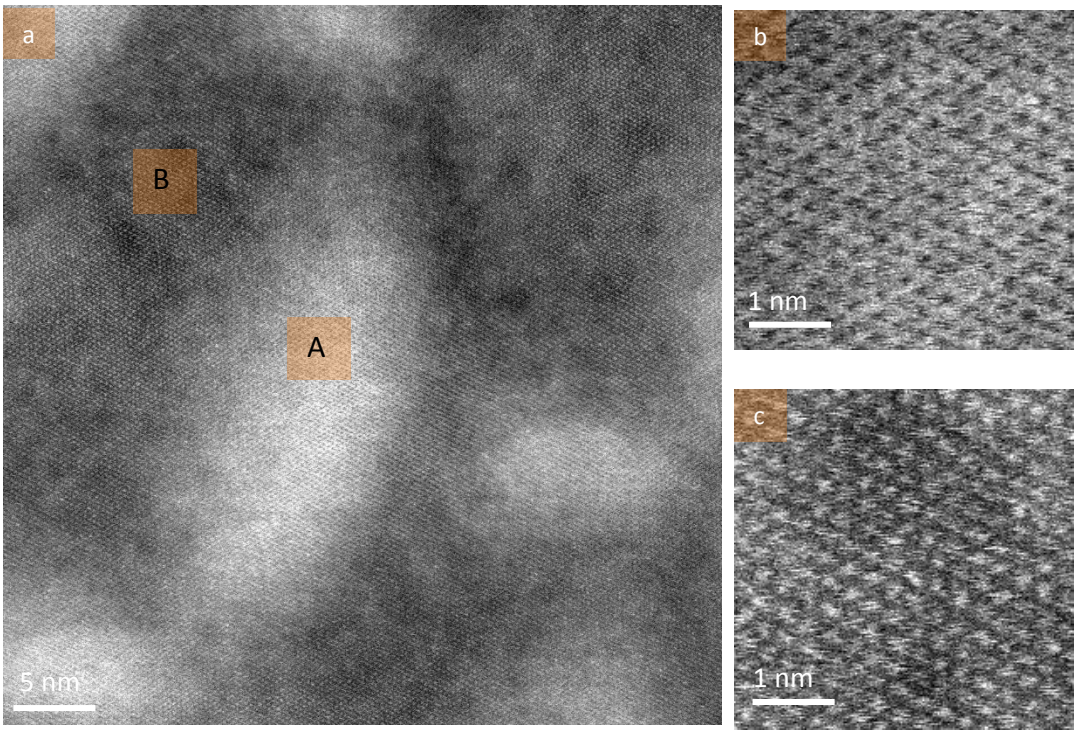

Figure 3.7: Moiré patterns in the HAADF-STEM image of layered 1T-TaS_2 on [001] zone-axis. (a) HAADF-STEM image showing different contrast in region A and region B. High magnification HAADF images of (b) region A showing a hexagonal structure and (c) region B showing a trigonal structure in (001) projection plane. Images recorded by R. Hovden.

To explore the relationship between image contrasts and stacking sequence of layered 1T-TaS_2, we simulated ADF-STEM images in a wide range of thicknesses and stacking sequences and incoherently averaged the ADF intensities (gray values) over one rectangular unit-cell of each image. Results are discussed in the following chapter.

3.4.2 CBED patterns

It is previously reported that CBED patterns can be exploited to determine the thickness and symmetry of various materials [9-12]. For example, by visually matching experimentally recorded and theoretically simulated CBED patterns, the thickness of crystalline silicon was determined with an error of about ± 1 nm [9]. Here, we used the same technique for determination of thickness and stacking sequence of imaged regions corresponding to experimental CBED patterns acquired from our 1T-TaS_2 sample.

Because the process of taking CBED patterns were parallel to HAADF-STEM imaging, experimental CBED patterns were recorded by scanning the electron probe across a region larger than a unit cell [10,21]. To reproduce the experimental conditions we simulated position-averaged CBED (PACBED) patterns. For example, a CBED pattern in Figure 3.8 corresponds to 10-layer 1T-TaS_2 with all-A stacking. It was calculated by incoherently averaging 20×34 CBED patterns simulated for different positions in one rectangular unit cell. Also, for each probe position, CBED patterns were averaged for 16 phonon configurations. In general, each CBED pattern in our work is an average of 10880 individual CBED patterns (Figure 3.9).

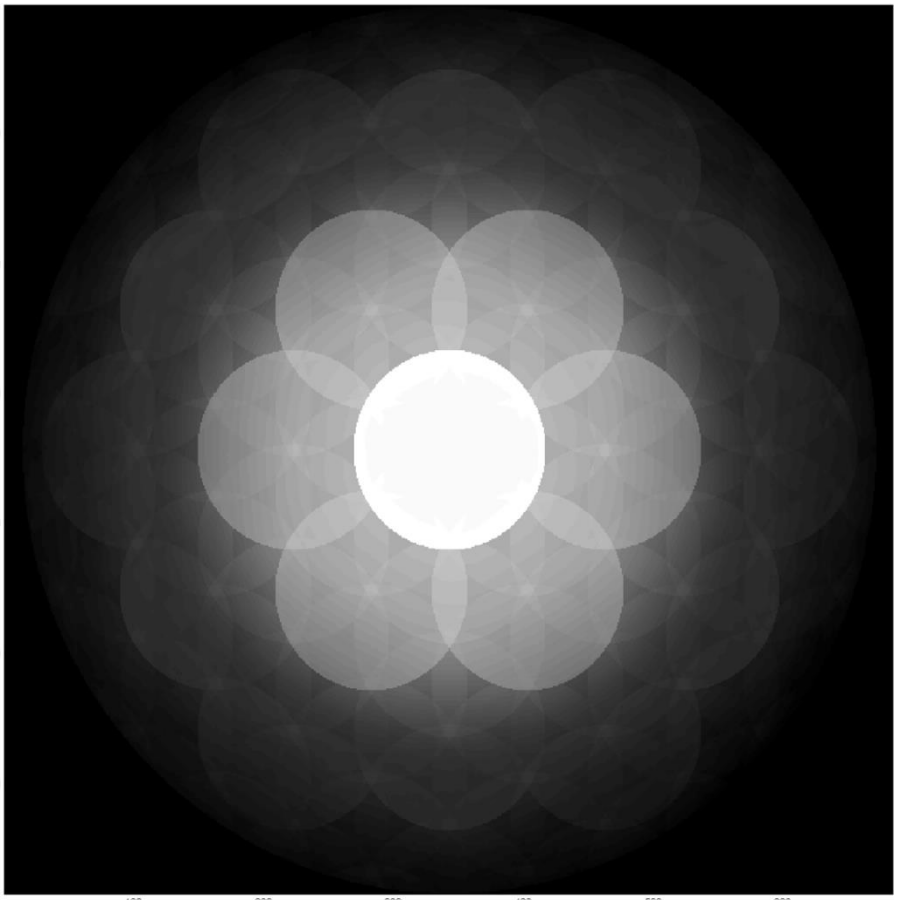

Figure 3.8: Position-averaged CBED pattern for 10-layer 1T-TaS_2 with all-A stacking.

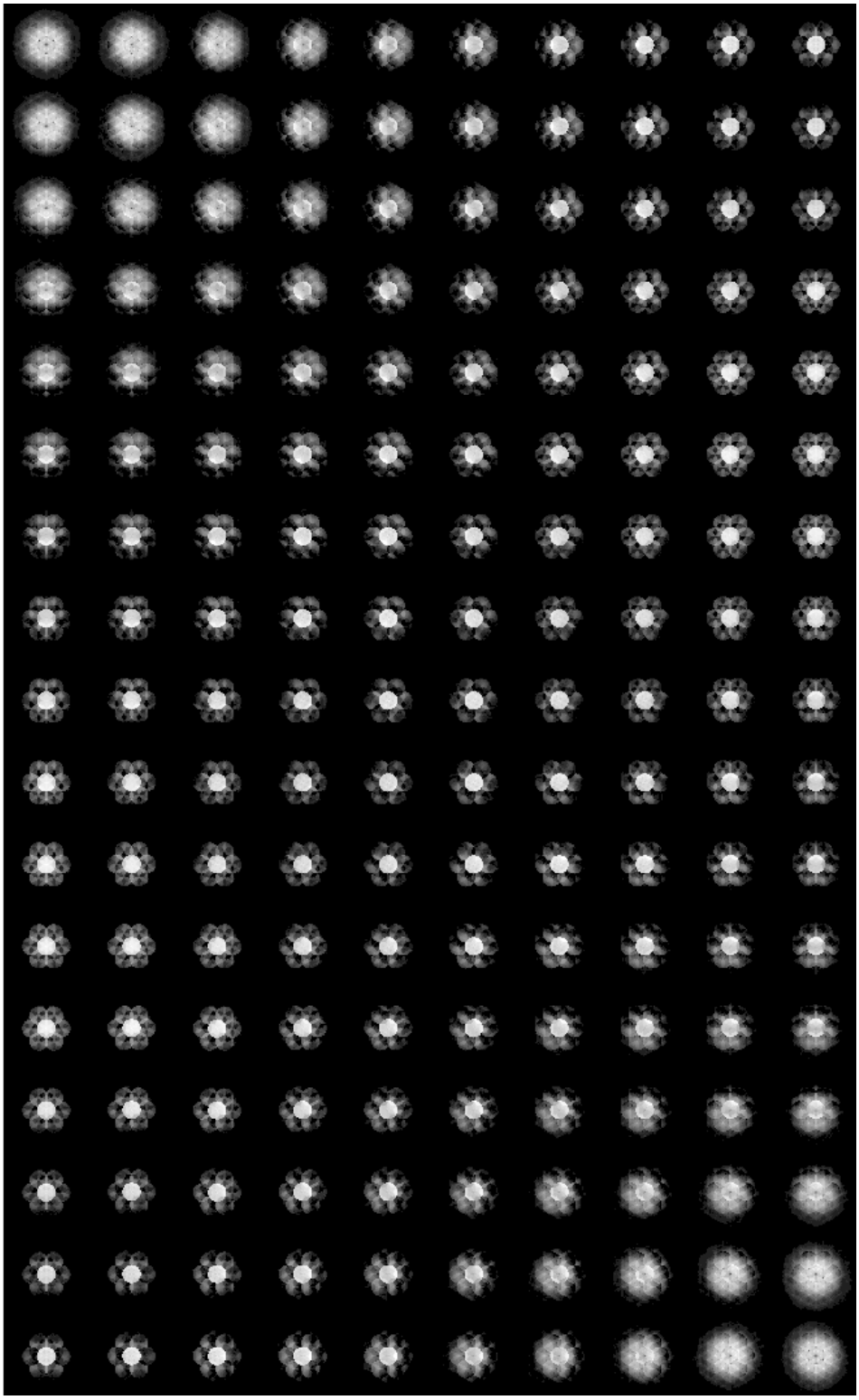

Figure 3.9: 10× 17 CBED patterns simulated for different positions in a quarter of rectangular unit cell for 10-layer 1T-TaS2 with all-A stacking.

CHAPTER 4

RESULTS AND DISCUSSION

In this Chapter, we shall discuss the simulation results of both HAADF-STEM images and CBED patterns for 1T-TaS_2 calculated using the multislice method.

4.1 HAADF-STEM images

As demonstrated in Chapter 2, the intensity of ADF-STEM images scales with atomic number Z, so atoms with larger atomic numbers appear brighter in HAADF images. In our case, Ta atoms (Z = 73) contribute more to the image intensity than sulfur atoms (Z = 16), thus the image contrast tracks variations in the Ta sites. Since the atomic layer of stacking directly affects the positions of Ta atoms in 1T-TaS_2, the image contrast can also be sensitive to changes in the stacking sequence. However, before studying the influence of stacking sequence on the HAADF image contrast, I will start with discussing simulated ADF-STEM images of 1T-TaS_2 stack with all-A stacking from single-layer (5.9Å) to 14 layers (82.6Å).

In this Chapter, the incident probe for all simulated ADF-STEM images was chosen according to the conditions of the aberration-corrected NION UltraSTEM 100. The aperture semi-angle was set to be 26 mrad and a 60 keV beam energy was applied to ADF-STEM image simulations. The atomic potentials and transmission functions were sampled on a 1024 × 1024 $pixel^2$ grid over 10.08 × 11.64 $Å^2$ (3 × 2 uc^2), thus the maximum scattering angle is far larger than the aperture size. Thermal diffuse scattering

is taken into account through the frozen phonon model [27,28]. Here, each ADF-STEM image was calculated by incoherently averaging over 16 phonon configurations with root-mean-square displacements in three-dimensions of 0.093 Å.

4.1.1 Two imaging models: Linear incoherent and multislice imaging simulations

Using the set of image simulation programs by E. J. Kirkland, we simulated HAADF-STEM images for all-A stacking 1T-TaS_2 with both linear incoherent and multislice imaging models. In its simplest picture, the linear incoherent imaging model can be interpreted as the linear convolution of the probe wavefunction with the atomic potentials weighted by $Z^{1.7}$ [30], where Z is the atomic number.

A comparison of the ADF-STEM image intensity calculated using the linear incoherent and multislice imaging model for all-A stacking 1T-TaS_2 from single-layer to 14 layers is presented in Figure 4.1. Each data point stands for the incoherently averaged intensity over one unit-cell normalized to the average intensity of the simulated ADF-STEM image for single-layer 1T-TaS_2.

Note that the relationship between averaged image intensities simulated with the incoherent imaging model and thicknesses is linear, as displayed in Figure 4.1. Thus the average intensity of *n* layers of 1T-TaS_2 is exactly *n* times that of the single-layer. Intensities are averaged over one unit-cell. The rectangular unit-cell as defined in Chapter 3.

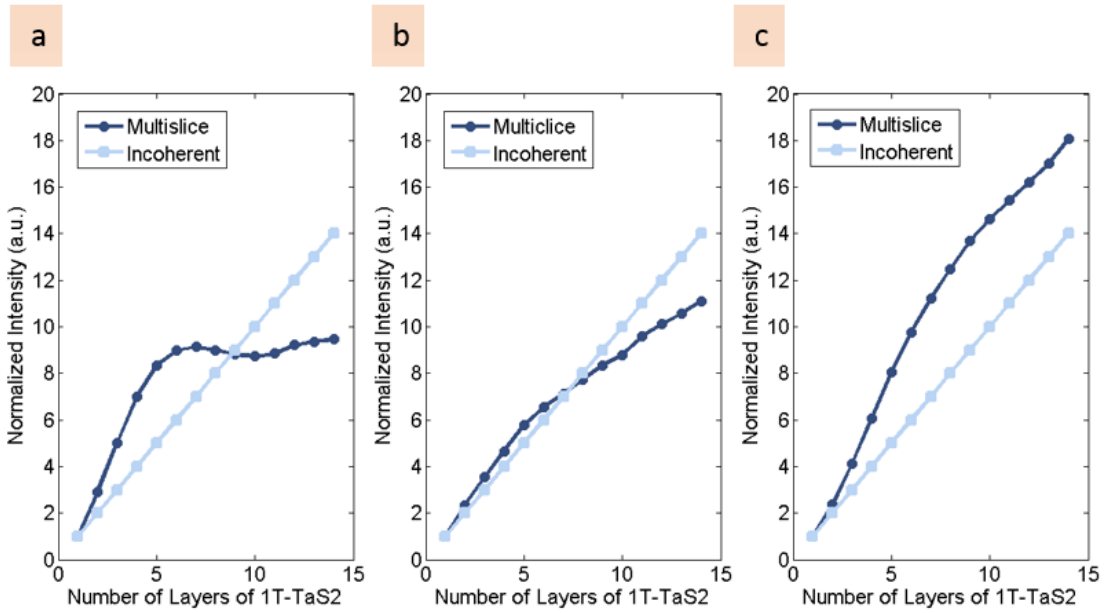

Figure 4.1: Normalized ADF intensity of 1T-TaS_2 varying with thickness and ADF detector angle. ADF intensity is calculated by both multislice simulations and the incoherent imaging model. ADF detector angles range from (a) 30 mrad to 90 mrad, (b) 50 mrad to 150 mrad and (c) 80 mrad to 240 mrad. All ADF intensities are computed by averaging gray values of one unit-cell in simulated images.

The multislice simulation, however, does not show the simple linear relationship between thickness and average ADF intensity of 1T-TaS_2 (Figure 4.1(a-c)). The ADF detector inner/outer angles were chosen over a wide range to include typical imaging modes from low-angle ADF (LAADF) to HAADF STEM.

It is noteworthy that the average ADF intensity calculated with detector angles from 30 mrad to 90 mrad is almost constant after approximately 6 layers (~35.4 Å). Since the final image intensity is integrated from all layers, the saturation of intensity in this thickness range suggests that electron scattering in the angular range from 30 mrad to 90 mrad is strongly reduced after a short distance of ~35.4 Å. And for the more realistic analysis, simulations of ADF signals at specific atomic columns are required. Although

it is also of interest, we would like to finish the thickness and stacking sequence measurement first.

Interestingly, when the number of layers (n) is smaller than 8, the multislice ADF intensity is always stronger than n times the single-layer's intensity (Figure 4.1(a,b)). For larger detector angles (Figure 4.1(c)), the normalized multislice ADF intensity for n ($n > 7$) layers of 1T-TaS_2 is still stronger than n, which is assumed to be due to the channeling effects as discussed in the following section.

4.1.2 Channeling effect

To study the channeling effect it is necessary to briefly introduce the incoherent imaging (II) model. In the II model, the ADF intensity on the detector plane can be simply interpreted as an integrated (over thickness) convolution of the specimen object function $T(\mathbf{x}, z)$ at each thickness z, and the electron probe function $\left|\Psi\left(\mathbf{x}_p, z\right)\right|^2$ [9, 31, 32]. If take detector geometry into account, then the final ADF image intensity is:

$$\mathrm{I}\left(\mathbf{x}_p\right) = \int G(k) \int_0^h \left|\Psi_p\left(\mathbf{x} - \mathbf{x}_p, z\right)\right|^2 \otimes T(\mathbf{x}, z)\, \mathrm{d}z\mathrm{d}k\,, \tag{4.1}$$

where $G(k)$ is the detector function in the ADF-STEM mode:

$$G(k) = \begin{cases} 1, & k_{inner} \le k \le k_{outer} \\ 0, & otherwise \end{cases}, \tag{4.2}$$

then the channeling signal $\frac{\mathrm{d}I}{\mathrm{d}z}\left(\mathbf{x}_p, z\right)$ can be defined as:

$$\frac{\mathrm{d}I}{\mathrm{d}z}(\mathbf{x}_p, z) = \int G(k)\left|\Psi_p(\mathbf{x}-\mathbf{x}_p, z)\right|^2 \otimes T(\mathbf{x}, z)\,\mathrm{d}k\,, \tag{4.3}$$

Former researches [9,33] reported that when incident electrons traveled in the specimen composed of zone-oriented atomic columns, instead of scattering they stayed in columns of atoms and led to enhancements of the final image signals. And the channeling signal can be calculated for chosen atomic columns with multislice simulations. Affected by the channeling effect, multislice ADF intensities of multilayer 1T-TaS_2 are enhanced under 8 layers (Figure 4.1(a,b)).

Figure 4.2 displays the average multislice ADF intensity of different stacking sequences as a function of thickness. For bilayer 1T-TaS_2, the average intensity of AA stacking is higher than that of AB stacking, which implies that the channeling along tantalum columns provide an enhancement in ADF signals for AA stacking. For tri-layer 1T-TaS_2, the channeling effect makes AAA and AAB stacking have higher average intensities than ABC stacking. However, when 1T-TaS_2 is thicker than 4 layers, the average ADF intensity shows a trend of $I_{A\ldots AA} < I_{A\ldots AB} < I_{A\ldots ABC}$. The physics behind this trend is still to be explored. And a possible approach to examine this conclusion would be calculating the probe shape of each column at each layer.

4.1.3 Influence of thickness and stacking sequence on HAADF-STEM image contrast

Moiré patterns in Figure 3.1(a) imply that structures formed by different stacking have a strong influence on the HAADF-STEM image intensity. This is consistent with what we concluded in Figure 4.3, which means that the hexagonal structure generated by

A…B…(C…) stacking results in a higher intensity compared with the trigonal structure of all-A stacking when the thickness is beyond 7 layers. Another simple conclusion is that the ADF intensity is in a positive correlation with the thickness of 1T-TaS_2.

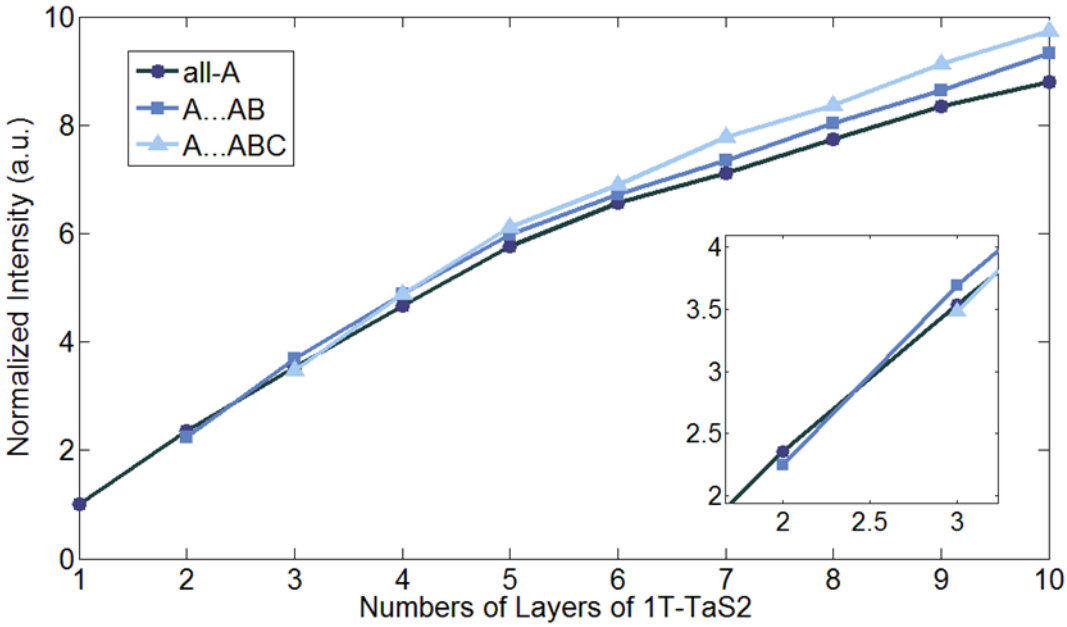

Figure 4.2: Normalized multislice ADF intensity for different stacking sequences of 1T-TaS_2 as a function of thickness. All ADF intensity is extracted by averaging gray values of one unit-cell in simulated images.

4.2 CBED patterns

The thickness of a variety of materials can be determined by directly matching experimental and simulated CBED patterns [9-12] as discussed in Chapter 3. In this chapter we will examine the simulation results of 1T-TaS_2 CBED patterns and the matching process to determine both thicknesses and stacking sequences of certain regions on 1T-TaS_2 films.

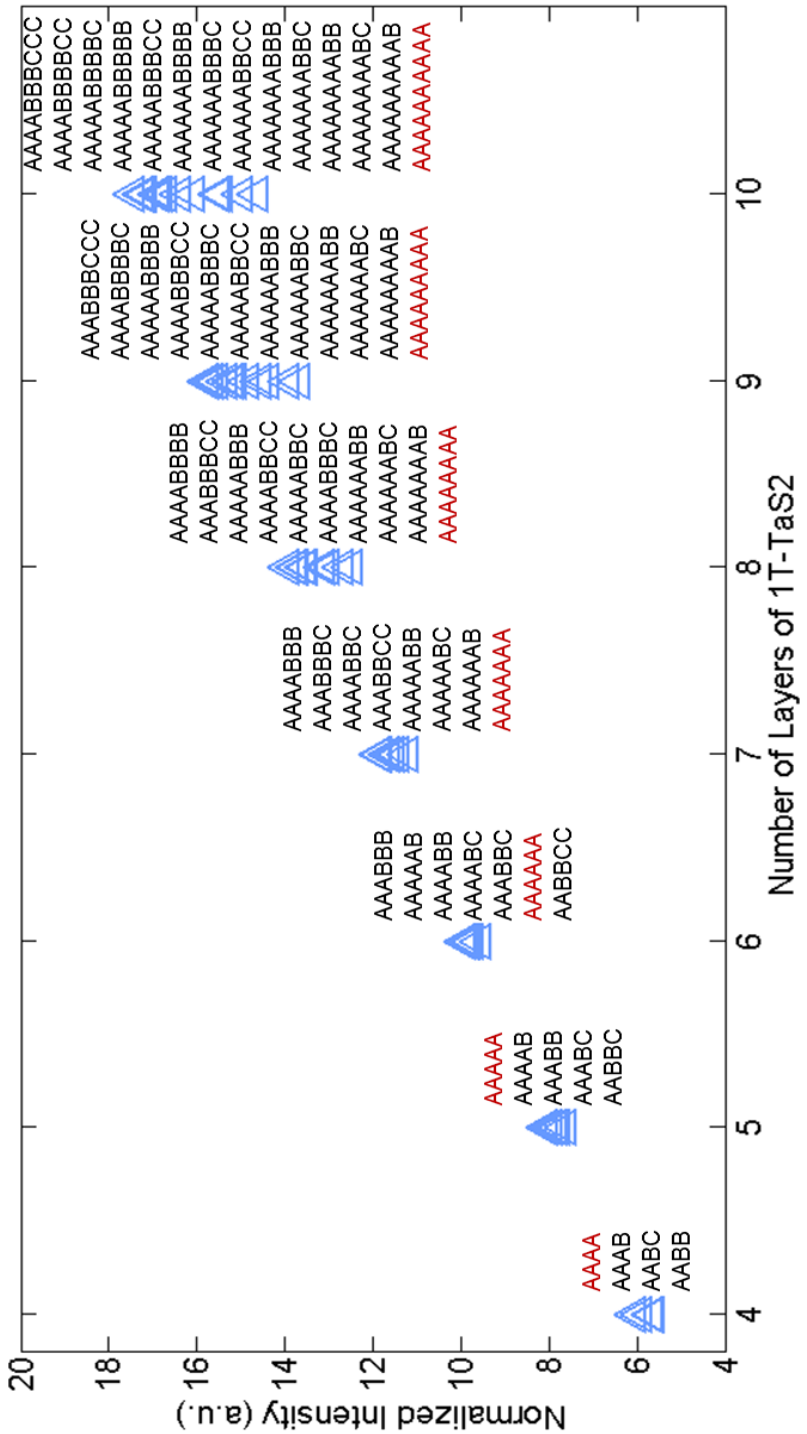

Figure 4.3: Normalized multislice HAADF intensity for different stacking sequences of 1T-TaS_2 as a function of thickness. Stacking sequences are labelled beside corresponding data points. All ADF intensity is extracted by averaging gray values of one unit-cell in simulated images.

To obtain CBED patterns with high resolution, a large supercell of 201.6×209.52 $Å^2$ (60×36 uc^2) on a 1024×1024 $pixel^2$ grid was chosen, which generated a small maximum angle of 62 mrad. But CBED patterns simulated on such grid contain sufficient features that are comparable with simulated patterns on a larger grid 2048×2048 $pixel^2$, which corresponds to a maximum angle about 125 mrad. Phonon scattering was also taken into account, so every simulated CBED pattern was incoherently averaged over 16 phonon configurations.

4.2.1 Symmetries of experimental CBED patterns

Figures 4.4(a-d) shows experimentally recorded CBED patterns of different regions on the same 1T-TaS_2 flake, and Figures 4.4(e,f) are plan-view HAADF-STEM images taken in the same area of the corresponding CBED patterns. These CBED patterns are acquired simultaneously with HAADF-STEM images by scanning the probe rapidly across desired regions, therefore they can also be treated as position-averaged CBED (PACBED) patterns. Here the sampling size of experimental CBED patterns was set by STEM scanning set-up, whereas in simulations, the sampling size of PACBED patterns is determined by input parameters of programs.

According to the symmetry of CBED patterns we can divide Figures 4.4(a-d) into two groups. The first group is Figures 4.4(a,b) since they all have a six-fold axis of rotation, and the second group is Figures 4.4(c,d) due to their three-fold rotational symmetry. Note that in the case of BL 1T-TaS_2, the top-down view of the AA stacking has a six-fold axis of rotation (Figures 3.1(a)), and the structure of AB stacking has a

three-fold axis of rotation (Figures 3.1(b)). If we assume that the CBED patterns reflect the sample's symmetries, then the CBED patterns of all-A stacking should also have six-fold symmetry. Before calculating CBED pattern for specific stacking sequence, some essential parameters for simulations should be considered.

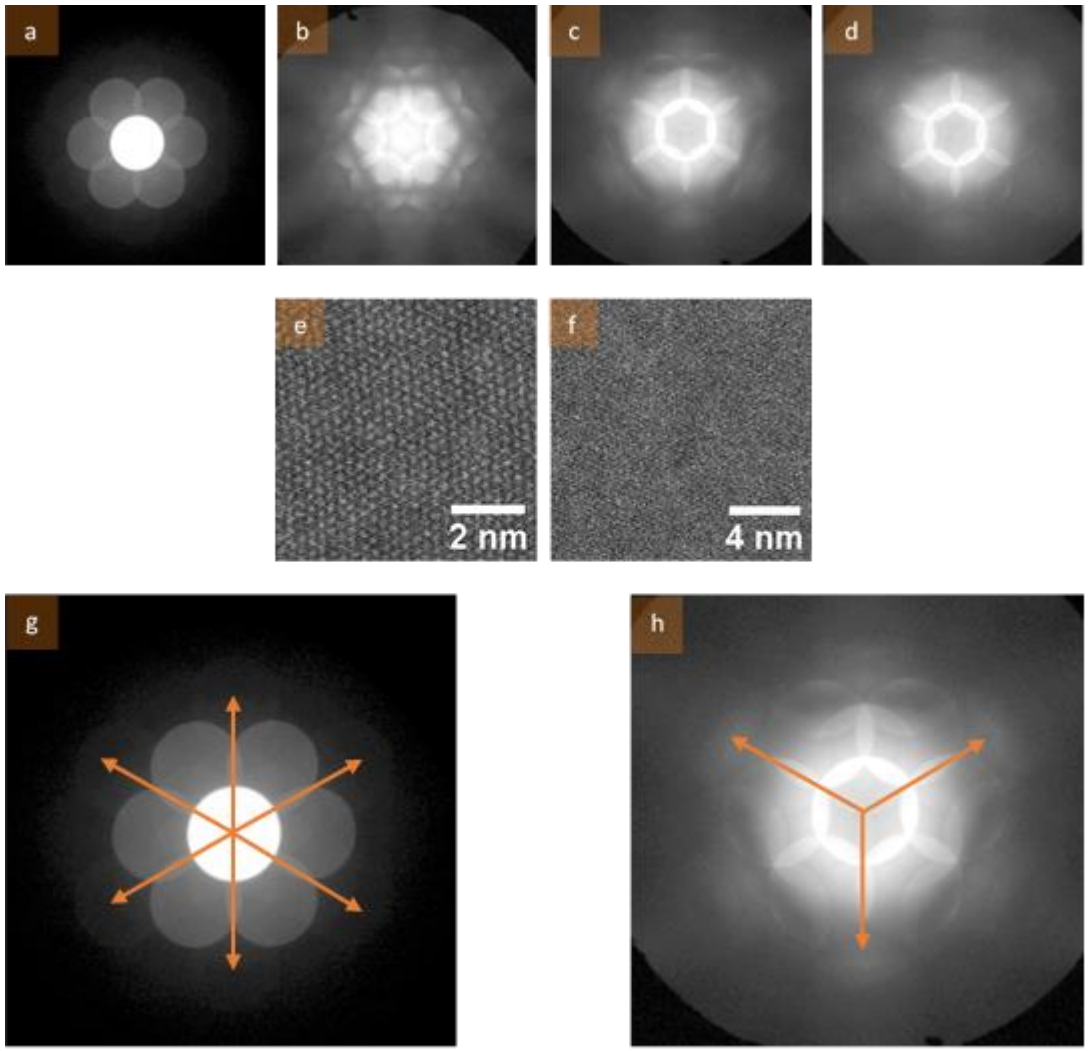

Figure 4.4: Experimentally recorded (a-d) CBED patterns and (e,f) HAADF-STEM images acquired from the same 1T-TaS_2 flake. (g) shows that the CBED pattern in (a) has a six-fold rotational symmetry while (h) implies that the CBED pattern in (c) has a three-fold rotational symmetry. HAADF-STEM images (e) and (f) correspond to CBED patterns in (b) and (c), respectively.

4.2.2 Sampling

In experiments the imaged area is sampled by setting up the pixel size. However, in simulations the image is calculated in a $N_x \times N_y$ rectangular grid (Figures 4.5), where N_x and N_y are numbers of pixels in x and y directions, respectively. In full multislice simulations, more sampling leads to more accurate calculations but we always need to consider the time cost in practice. Insufficient sampling, however, fails to produce reliable images due to aliasing [23].

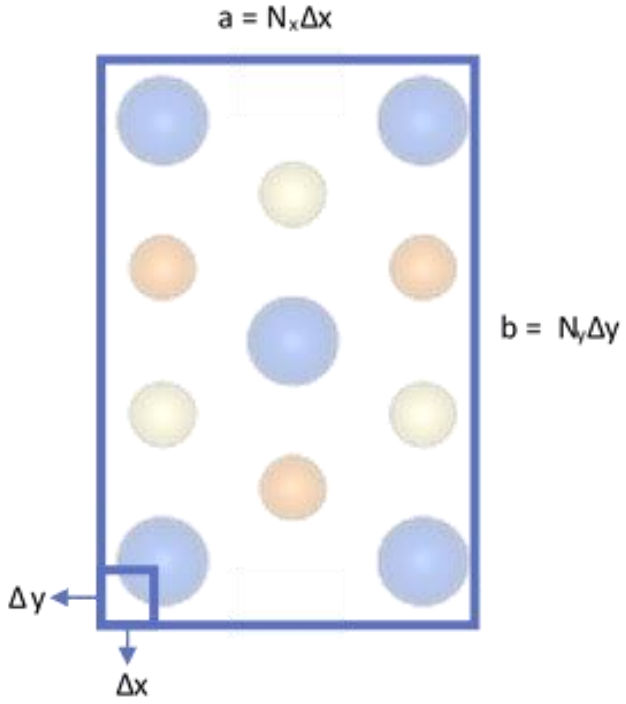

Figure 4.5: Schematic of the sampling process of a structure (a unit-cell in our case) over a size of $a \times b$. The calculated image has $N_x \times N_y$ pixel^2, and each pixel has a size of $\frac{a}{N_x} \times \frac{b}{N_y}$ in real space.

Figures 4.6 display simulated CBED patterns for 10 layers of 1T-TaS_2 with different sampling from 2×3 to 100×173. For a sampling of 100×173, the sampling size for one pixel is 3.36Å/100 = 3.36×10^{-2}Å, which is small enough for a good approximation of infinite sampling. But the calculation time for such configuration (16 phonon modes) is several days, hence we need to find the balance point between quality of simulated images and computation time. As shown in Figures 4.7, by putting images side by side, CBED patterns with sampling beyond 10×17 for one unit cell (3.36×5.82 Å^2) in the projection plane are found to match the pattern with 100×173 sampling. Therefore, for accurate calculations and reasonable computation time, a sampling of size 20×34 was chosen in the following simulations.

4.2.3 Influence of the objective aperture size

The size of the objective aperture plays a critical role in the appearance of CBED patterns. Weyland and Muller [34] pointed out that by measuring the diameter of the diffraction disc, d, and the disc spacing D, the convergence semi-angle, α, can be calculated by a simple equation as:

$$\frac{d}{D} = \frac{\alpha}{\theta_{\mathrm{bragg}}}, \tag{4.4}$$

where θ_{bragg} is the Bragg angle for a particular reflection.

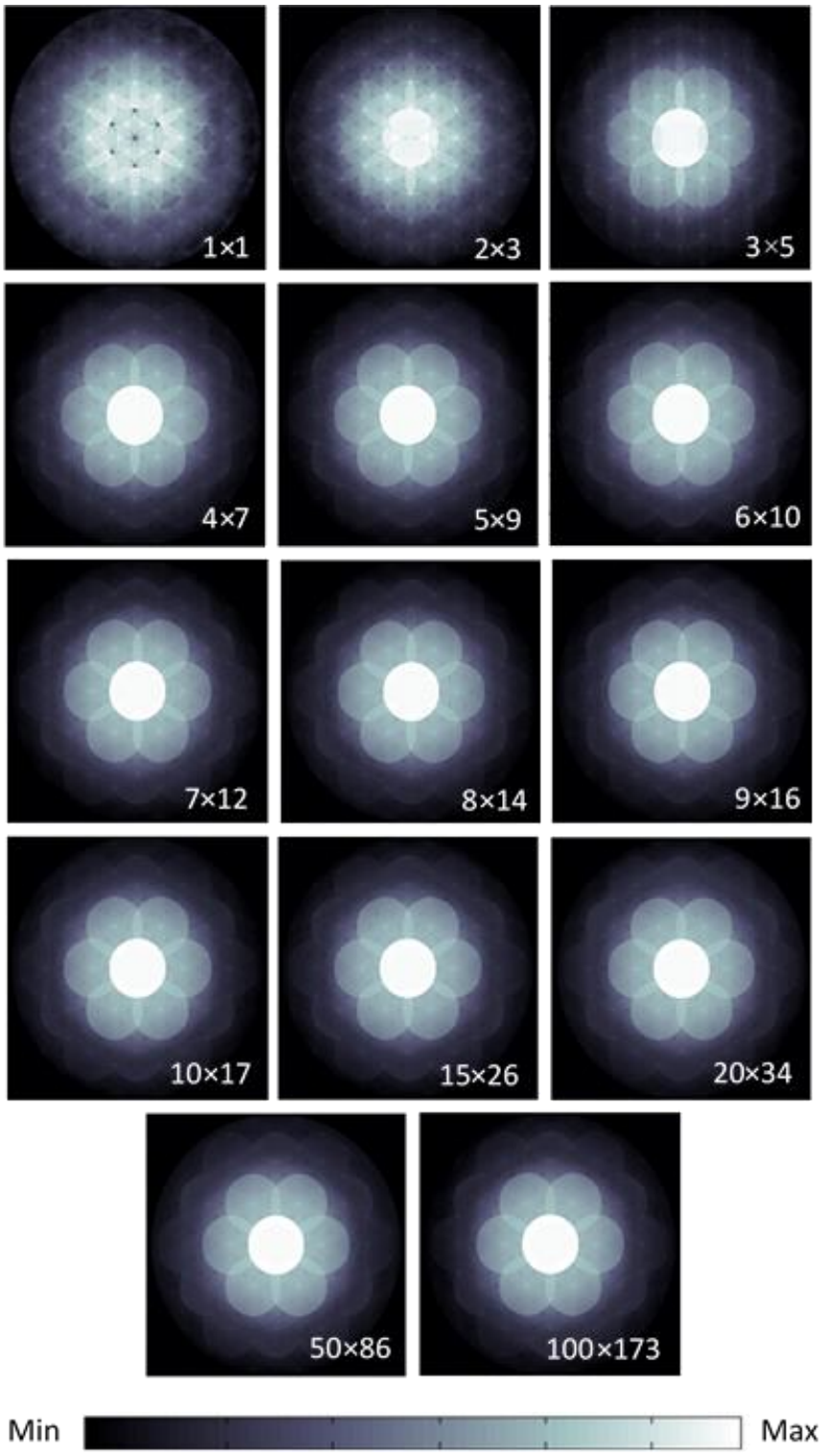

Figure 4.6: Simulated CBED patterns for 10 layers of 1T-TaS2 with all-A stacking along [001] at different samplings from 2×3 to 100×173. All simulated CBED patterns are displayed on a logarithmic scale.

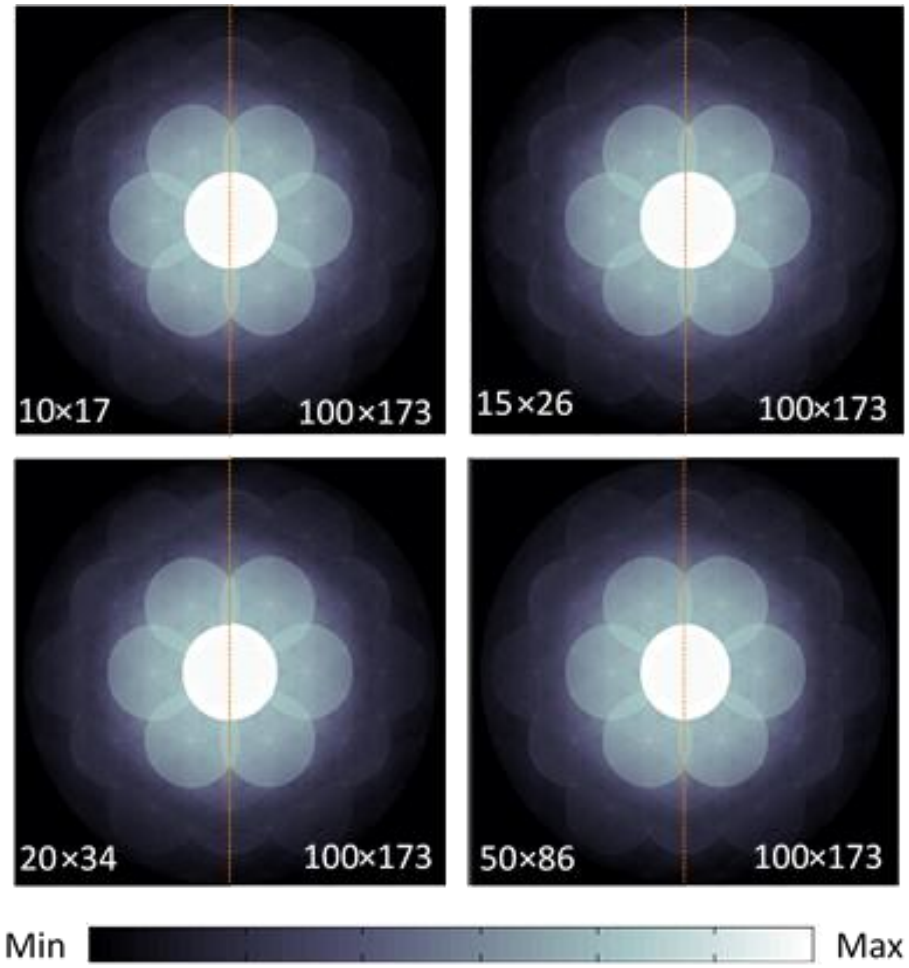

Figure 4.7: Simulated CBED patterns for 10 layers of 1T-TaS_2 with all-A stacking along [001] in different samplings from 10 ×17 to 50 ×86 (left) compared with a sampling of 100 ×173 (right).

Figure 4.8 reveals distinct features of CBED patterns with different objective aperture sizes. Hence calculating CBED patterns with the appropriate aperture size is crucial for the purpose of thickness and stacking sequence determination. For STEM performed on a 200 kV FEI Tecnai F20 SuperTWIN, the optimum convergence semi-angle is 9.6 mrad. The [34] experimental CBED patterns were recorded with a slightly smaller aperture of 9.2 mrad, which was also used for our CBED simulations. Note that as the aperture size increases the detailed features in CBED patterns become less visible,

thus for aberration corrected microscopes such as the fifth-order aberration corrected NION UltraSTEM 100 with large convergence semi-angle, thickness and stacking sequence determination using CBED patterns is more difficult. The convergence angle can of course be reduced at the expense of spatial resolution.

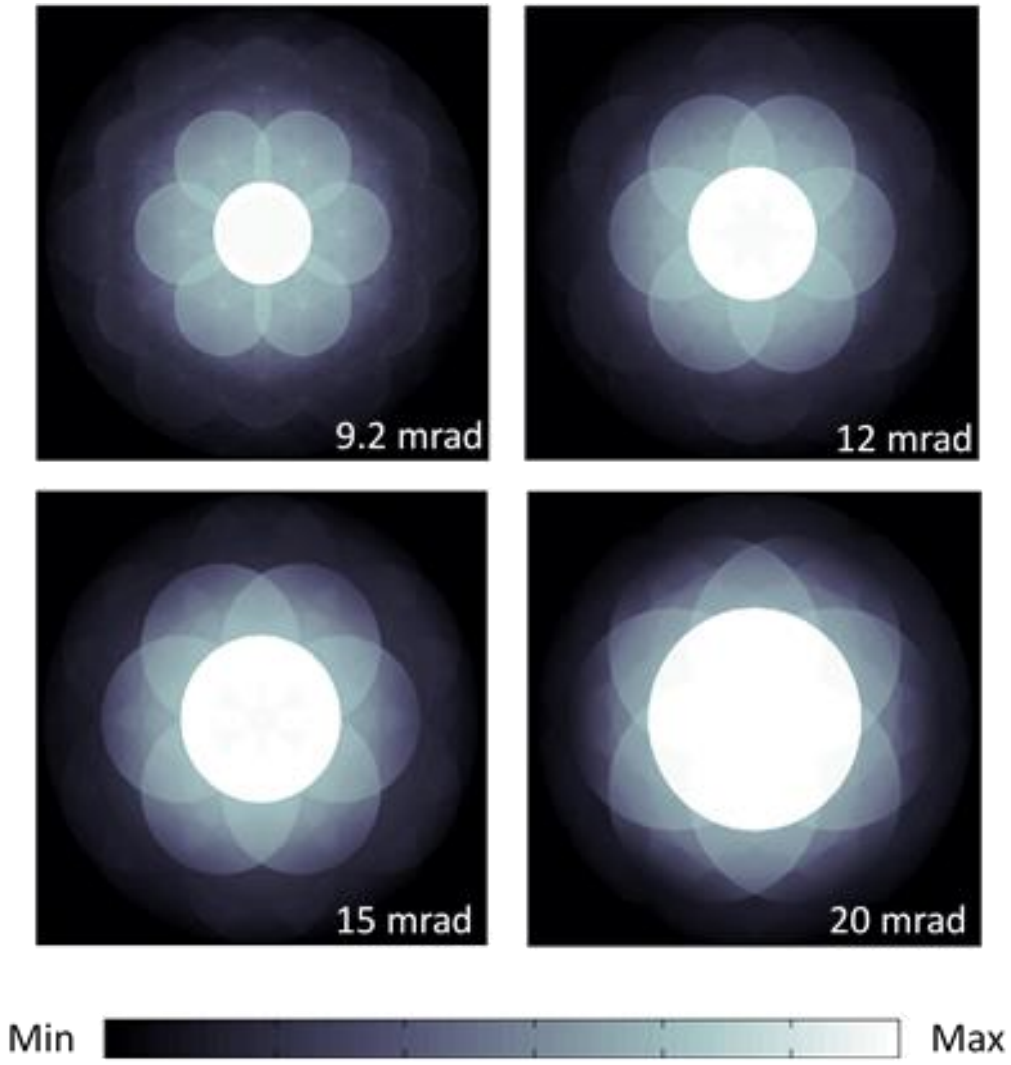

Figure 4.8: Aperture size-dependence of simulated CBED patterns. All patterns are calculated for 10 layers of 1T-TaS_2 with all-A stacking along [001].

4.2.4 Thickness determinations of all-A-stacking

As predicted, the CBED patterns of all-A stacking (bulk-like) has a six-fold axis of rotation (Figure 4.10). On the logarithmic scale, distinct features contained in low-order discs in each pattern provide rich information for thickness determination. Especially, since the dark ring has a hexagonal shape in the experimental CBED pattern (Figure 4.9(b)), the thickness of the imaged area could be narrowed down to a range of 35 ± 1 layers, and the error is determined by comparing experimental and simulated CBED patters side by side (Figure 4.11). Similarly, the thickness of the selected area relative to the experimental CBED pattern in Figure 4.12 was determined to be 4 ± 2 layers. Thus, using the CBED thickness measurement technique could be determined within an error as small as ~ ±1 nm, and such accuracy is compatible with other thickness techniques including the atomic force microscopy.

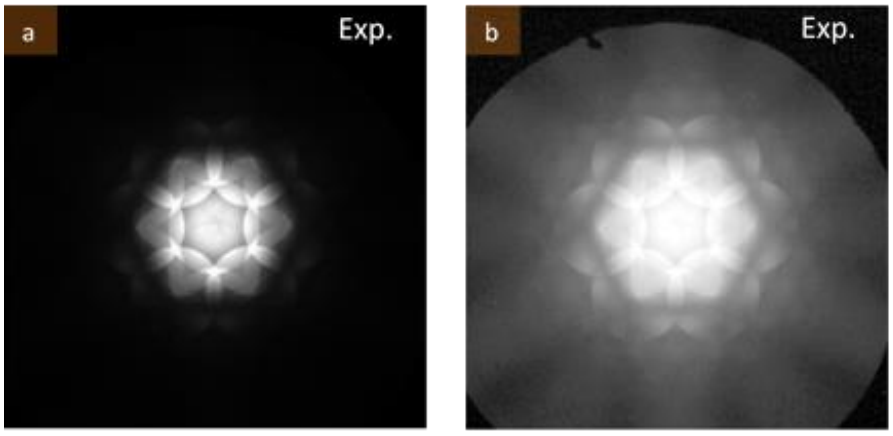

Figure 4.9: Experimental CBED patterns of 1T-TaS_2 along [001] on (a) original and (b) logarithmic scale. The original CBED pattern provides detailed features in the central disc while more information at low intensity is disclosed by the CBED pattern on logarithmic scale.

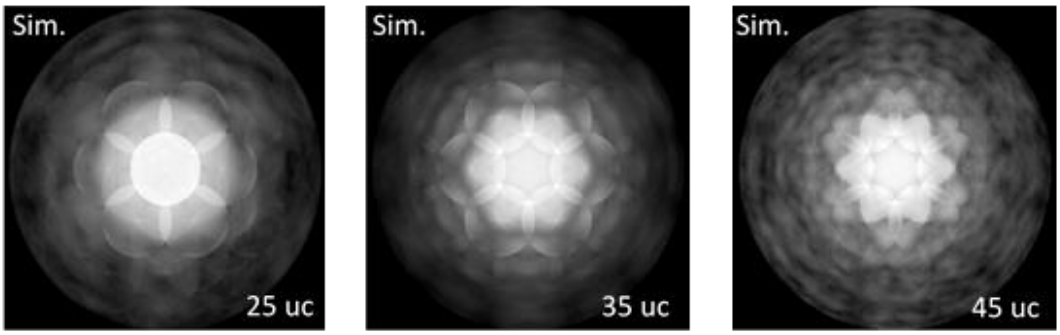

Figure 4.10: Simulated CBED patterns for different thicknesses of 1T-TaS_2 with all-A stacking along [001] on logarithmic scale.

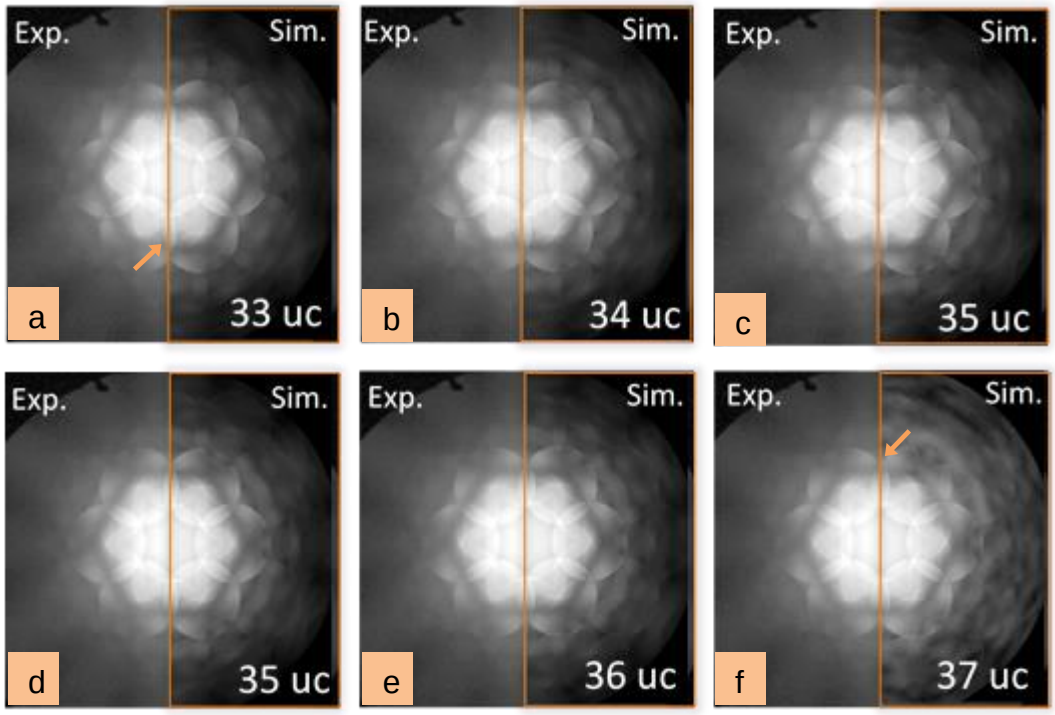

Figure 4.11: Visual comparisons between the experimentally recorded CBED patterns (left half of (a)-(f)) and simulated CBED patterns with different thicknesses (right half of (a)-(f)). The thickness for corresponding area of 1T-TaS_2 is determined by matching the hexagonal ring in both CBED patterns. Obvious mismatches of hexagonal rings are labelled in (a) and (f) with arrows.

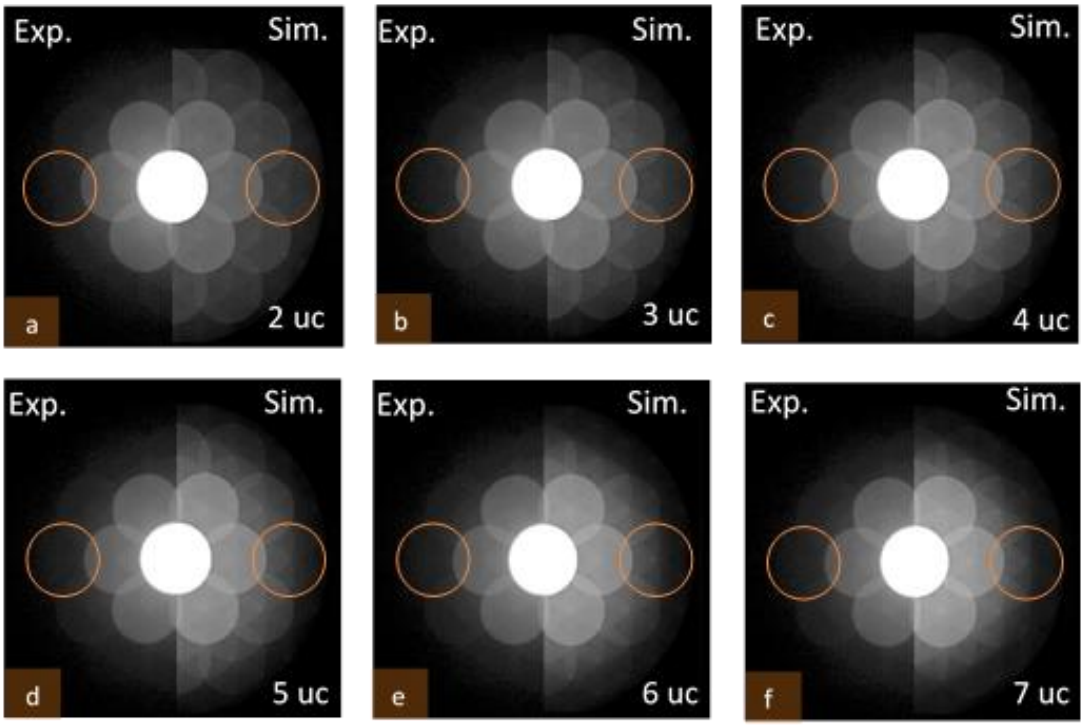

Figure 4.12: Visual Comparisons between the experimentally recorded CBED patterns (left half of (a)-(f)) and simulated CBED patterns with different thicknesses (right half of (a)-(f)). The thickness of the 1T-TaS_2 is determined by matching the contrast in circled disc in both CBED patterns.

4.2.5 Stacking sequence determination from CBED patterns with three-fold rotational symmetry

Figure 4.13 shows experimental CBED patterns with three-fold rotational symmetry acquired from different regions of 1T-TaS_2, and these patterns don't match any simulated CBED patterns of all-A stacking. Therefore, we started from calculating the simplest case other than bulk-like stacking, which is A…B… stacking, i.e. a stack of layers with A stacking followed by a stack of layers with B stacking.

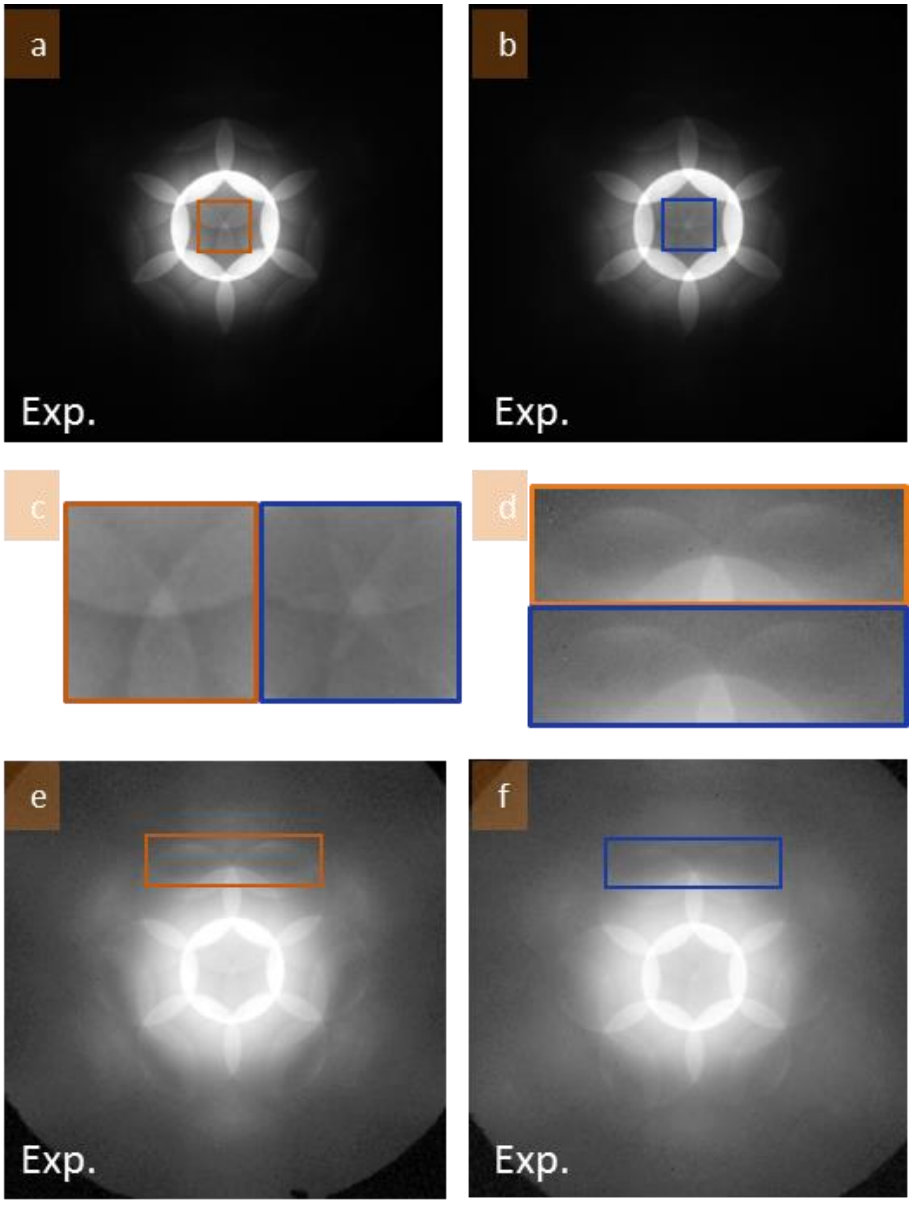

Figure 4.13: Experimental CBED patterns of 1T-TaS_2 along [001] displayed on (a,b) original and (e,f) logarithmic scale. The original CBED pattern provides (c) detailed features in the central disc while (d) more information at low intensity is disclosed by CBED patterns on logarithmic scale. Magnified details in central disc outlined by squares in (a) and (b) are shown in (c). (d) displays magnified images of lobes from the regions indicated by rectangles in (e) and (f) for different CBED patterns. CBED patterns recorded by R. Hovden.

Tracking features in the central disc of original experimental CBED patterns can contribute to stacking sequence determination, and details of diffracted dark lines exhibited by CBED patterns on logarithmic scale are exploited for thicknesses identification.

Here, we need to clarify the term "stacking sequence" as used in this section. Since calculating all possible configurations of stacking will take a huge amount of time, we focus on the simplest case, intentionally overlooking all effects in z-direction. Therefore, the stacking sequence is only referred to numbers of A-layers and B-layers for our current simulations, which means in fact we are not able to extract the exact stacking sequence from experimental CBED patterns.

Here we will demonstrate two examples for stacking sequence and thickness determination of A…B… stacking. Figure 4.14 shows the influence of stacking sequence and thickness of A…B…stacking on simulated CBED patterns. By matching detailed features in the central disc and the shape of diffracted dark lines of experimental CBED patterns, the thicknesses of two regions on a 1T-TaS_2 sample are determined (Figure 4.15).

4.3 Limitations of stacking sequence determinations

As mentioned previously, the exact stacking sequence cannot be determined due to following reasons.

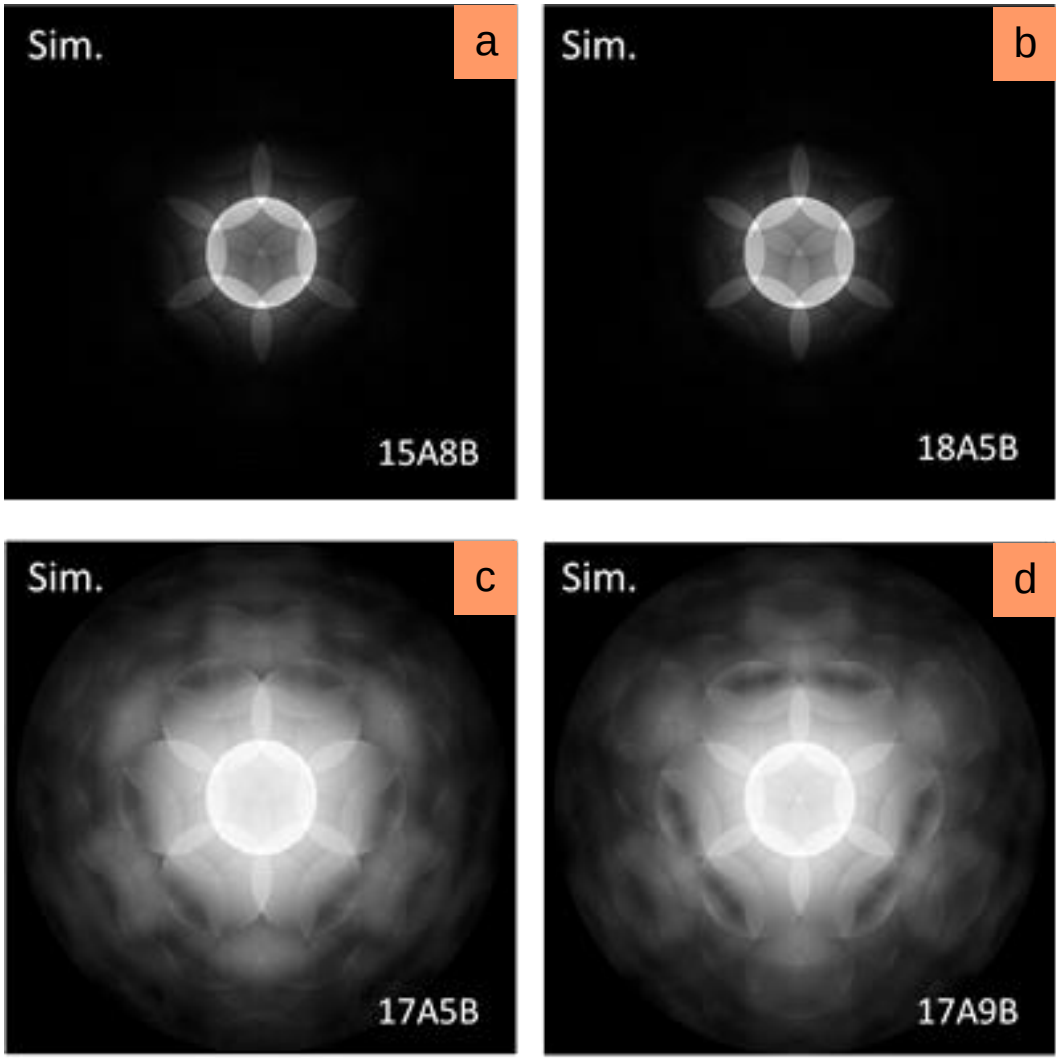

Figure 4.14: Simulated CBED patterns of 1T-TaS_2 for different stacking sequences along [001] on (a,b) original and (c,d) logarithmic scale. CBED patterns in (a) and (b) correspond to the same crystal thickness, but different stacking sequences 15A8B and 18A5B, respectively. CBED patterns in (c) and (d) are calculated with the same number of layers in stack A, but different numbers of layers in stack B.

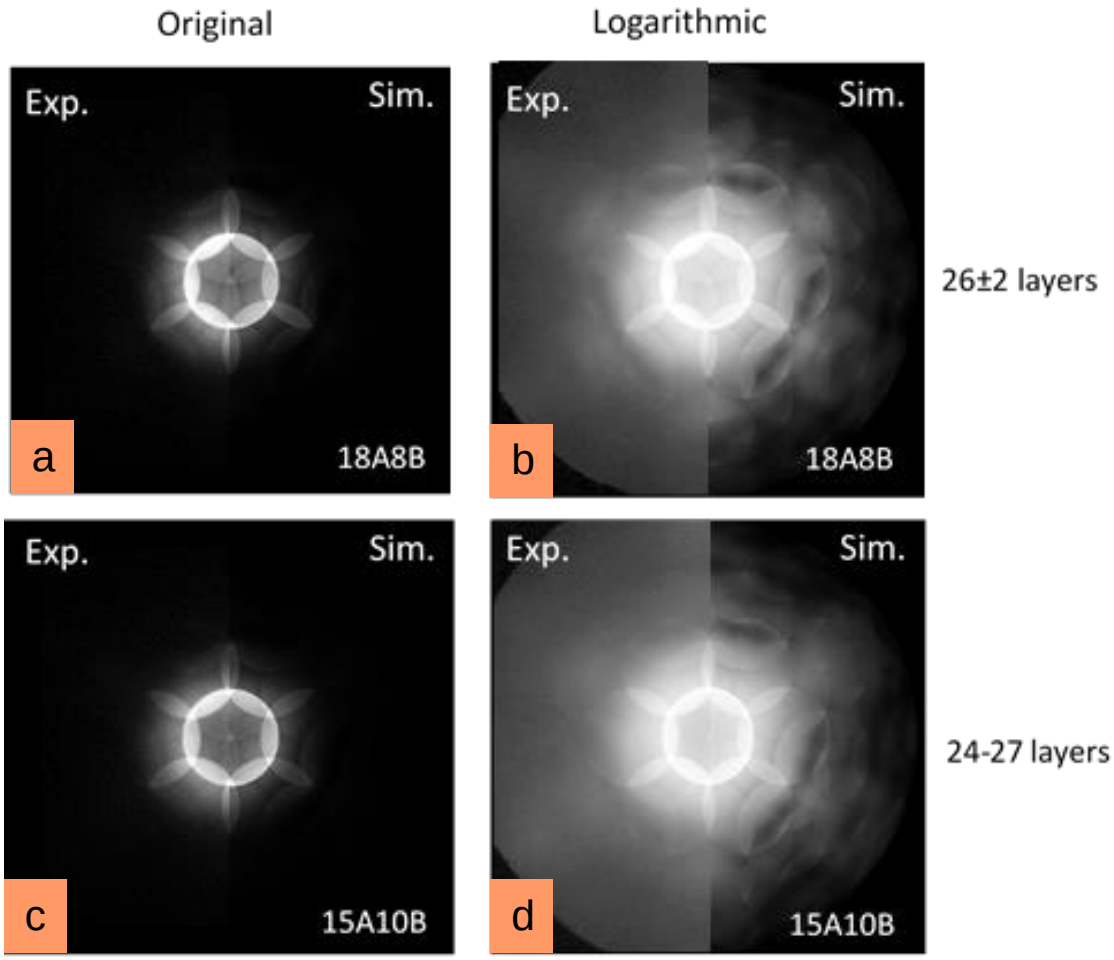

Figure 4.15: Comparisons between experimentally recorded CBED patterns (left half of (a)-(d)) and simulated CBED patterns (right half of (a)-(d)). The thicknesses for corresponding areas of 1T-TaS_2 are determined by matching experimental and simulated CBED patterns on (a,c) original and (b,d) logarithmic scale. The thicknesses of regions (a,b) and (c,d) were determined to be 26±2 layers and 24 to 27 layers, respectively.

4.3.1 A…B… stacking and ABAB…AB stacking

In practice, the difference between A…B… stacking and ABAB…AB stacking (Figure 4.16) cannot be ignored because the imaging process is not purely incoherent, which leads to obstacles for extracting the exact stacking sequence from each CBED pattern.

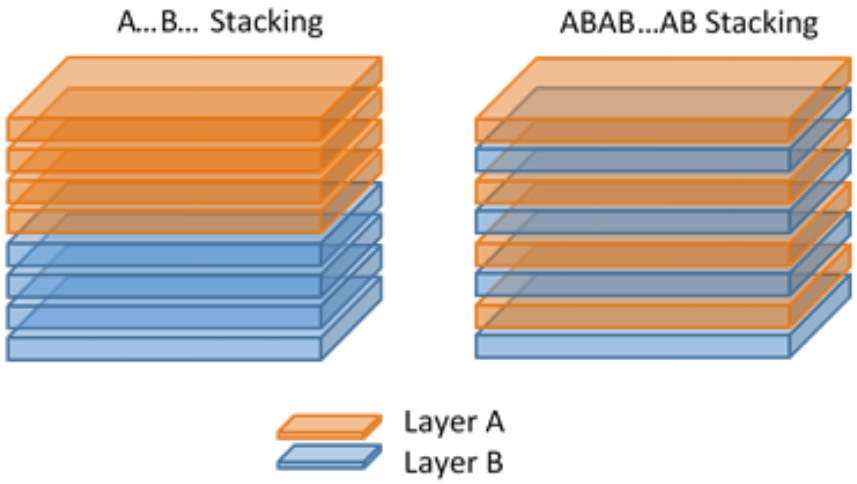

Figure 4.16: Schematic illustration of A…B… stacking and ABAB…AB stacking.

For instance, mathematically, there are C_{26}^{13} ~10^7 possible stacking sequences with 13 layers of A and 13 layers of B. Obviously, it is not practical to calculate all possible arrangements and compare them with the experimental CBED pattern.

As shown in Figure 4.17, while both CBED patterns correspond to sample areas of 13 layers of A-stacking and 13 layers of B-stacking, distinct features are observed in these two CBED patterns. Although this result can be predicted because CBED patterns are very sensitive to variations in structures and symmetries of materials, it brings uncertainty to the exact determination of stacking sequences.

Note that although the structure of ABAB…AB stacking in projection plane (001) has a three-fold axis of rotation, the corresponded CBED pattern exhibits a six-fold rotational symmetry, and the reason behind such unexpected result is to be studied in the near future.

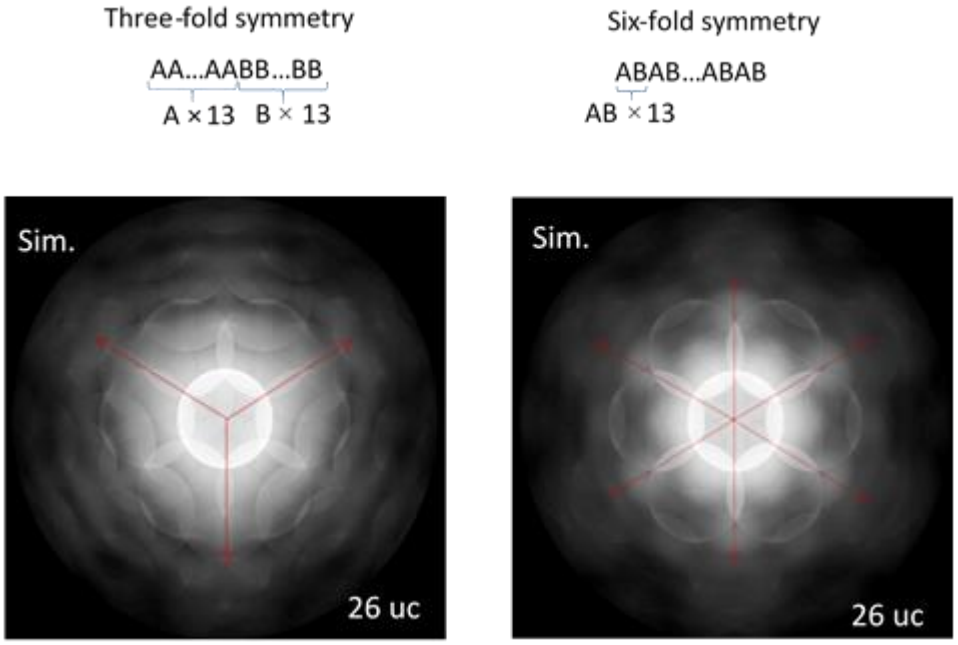

Figure 4.17: Simulated CBED patterns of 26-layer 1T-TaS_2 for different stacking sequences along [001] on logarithmic scale. (a) A...B… stacking. (b) ABAB…AB stacking.

4.3.2 Visual comparisons between A…B… stacking and A…B…C... stacking

Although CBED patterns are sensitive to changes in structure (symmetry), difficulties still exist when it comes to visual comparisons of A…B… stacking and A…B…C…stacking. Figure 4.18 shows calculated CBED patterns for A…B…stacking (13A13B and 16A10B) and A…B…C…stacking (13A12B1C and 13A10B3C). Although the CBED pattern for 16A10B stacking can easily be distinguished from two

A…B…C…stacking CBED patterns, the difference between 13A12B1C stacking and 13A10B3C stacking is small and not sufficient for stacking sequence determination. It is noteworthy that in central discs of CBED patterns for 13A12B1C stacking and 13A10B3C stacking, lobe 1, 3 and 5 are brighter than lobe 2, 4 and 6 (Figure 4.18(b)). On the contrary, lobe 2, 4 and 6 are brighter than other three lobes for the CBED pattern of 16B10A stacking. This finding might be an important clue for stacking sequence determination when layer-C is involved. Meanwhile, a quantitative comparison between simulated and experimental CBED patterns might be required when C stacking is introduced.

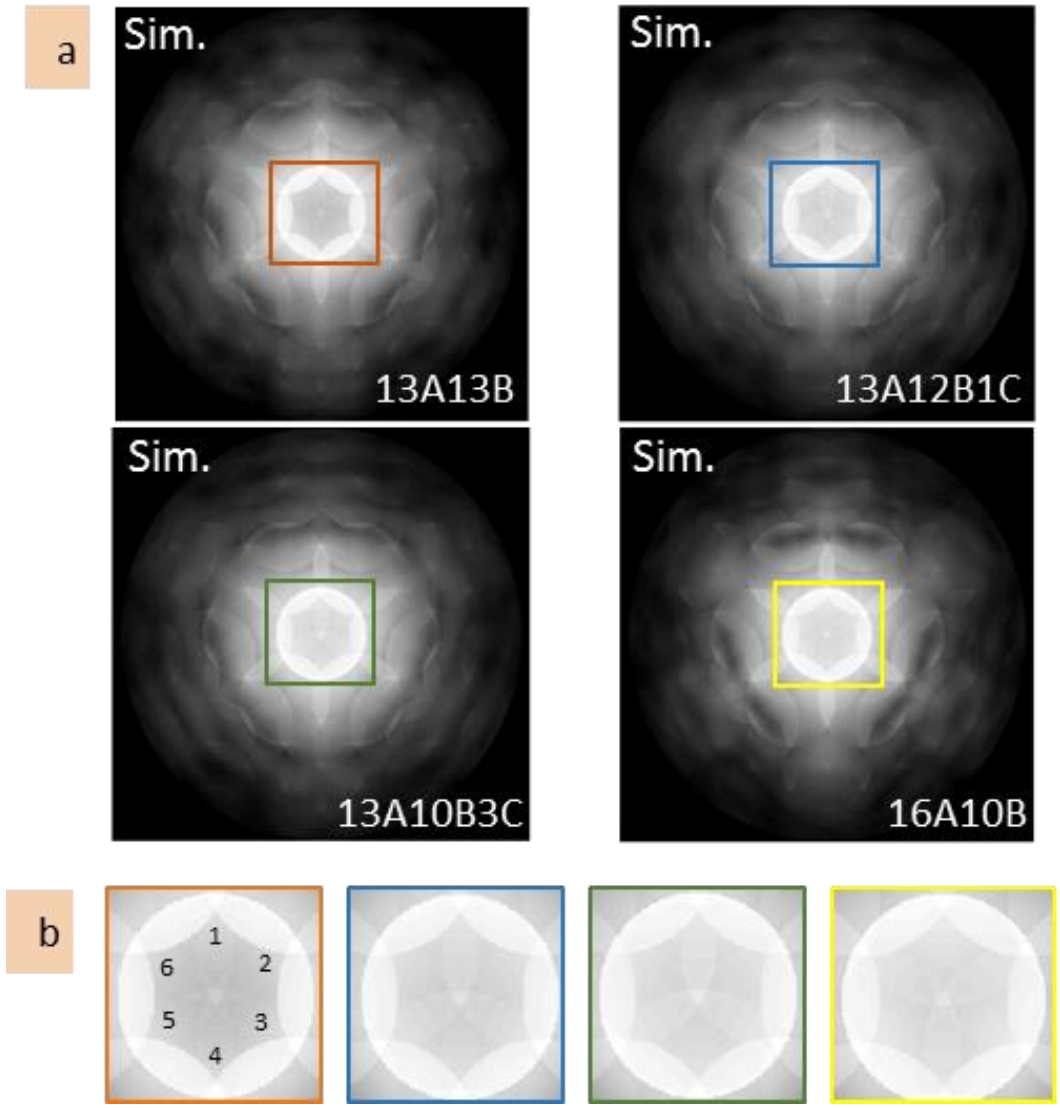

Figure 4.18: Simulated CBED patterns of 26-layer 1T-TaS_2 for different stacking sequences along [001] on logarithmic scale. (b) Magnified images of lobes in the central discs of CBED patterns in (a).

CHAPTER 5

CONCLUSIONS AND FUTURE WORK

5.1 Conclusions

Using image simulations we proved that the hexagonal structure in the (001) projection plane of 1T-TaS_2 thin film was caused by shifting all Ta sites in one layer with a bond-length relative to other layers. Image simulations were also used to study the influence of thickness and stacking sequence on HAADF-STEM images of 1T-TaS_2 (001) projection plane. Full-multislice simulations suggest that the average intensity of HADDF-STEM images will increase as the thickness of 1T-TaS_2 increases from single-layer (~5.9Å) to 14 layers (~82.6Å). Compared with the trigonal structure of Ta sites in the (001) projection plane, the hexagonal structure generated by shifting between layers produces higher average intensity in HAADF-STEM images.

Various thicknesses were extracted from experimentally recorded CBED patterns of all-A stacking (bulk-like) 1T-TaS_2 by visually matching experimental and simulated images. Although more quantitative thickness determination should be applied with pattern matching algorithms, the accuracy of visual comparisons has been comparable with or better than other techniques (~ ± 1 nm). While uncertainties exist in the determination of exact stacking sequences, significant influences of different stacking sequences (all-A stacking/A…B…stacking) were observed in both experiments and simulations.

5.2 Future work on this project

As mentioned in the abstract, our goal is to develop a reliable method to extract the thickness and stacking sequence of 1T-TaS_2 directly from experimentally recorded images. So far we have examined the determination of all-A stacking's thickness as well as distinct differences between all-A stacking and A...B…(C…) stacking by visual inspection of experimental and simulated CBED patterns. For more accurate image analyses, our further concern is to conduct quantitative comparisons rather than subjective visual comparisons. Other computationally inexpensive algorithms should also be applied to calculations of CBED patterns, like Bloch-wave simulations.

5.2.1 Quantitative comparison

In Chapter 4 we demonstrated comparisons between experimentally recorded CBED patterns and theoretically simulated CBED patterns. We call them "visual comparisons" because the matching process was essentially looking for agreement between measured and calculate images by visual inspection. However, visual comparison is subjective due to the variance of human eyes, judgements of consistency, and tolerance of differences.

For more detailed analysis we need a more quantitative comparison. Existing approaches of quantitative comparisons can be divided into two main branches: measuring the difference between observed images and simulated images, or calculating the cross correlation coefficient of two images. Here we will briefly discuss these two schemes of quantitative comparisons.

Barry [35,36] brought up the description of Chi-square (χ^2) to describe the difference between two images:

$$\chi^2 = \frac{1}{N_x N_y} \sum_{i,j} \left[f_{\exp}(x_i, y_j) - f_{\sim}(x_i, y_j) \right]^2 / \sigma_{ij}^2 , \qquad (5.1)$$

where N_x and N_y are numbers of image pixels in x and y directions, respectively. In our case, $f_{\exp}(x_i, y_j)$ and $f_{\sim}(x_i, y_j)$ are gray values of pixel (i, j) in experimental images and simulated images, respectively. And σ_{ij} represents the error corresponded to pixel (i, j). The standard of a good match should then be defined as $\chi^2 \sim 1$ [23].

Thust et al. [37], and Möbus et al. [38] proposed to use the cross correlation coefficient defined as:

$$C_{\text{corr}}(f_{\exp}, f_{\sim}) = \frac{\sum_{i,j} (f_{\exp}(x_i,y_j) - \langle f_{\exp} \rangle)(f_{\sim}(x_i,y_j) - \langle f_{\sim} \rangle)}{\sqrt{\sum_{i,j} (f_{\exp}(x_i,y_j) - \langle f_{\exp} \rangle)^2 \sum_{i,j} (f_{\sim}(x_i,y_j) - \langle f_{\sim} \rangle)^2}} , \qquad (5.2)$$

where $\langle f_{\exp} \rangle$ and $\langle f_{\sim} \rangle$ stands for average intensities (gray values) of $f_{\exp}(x_i, y_j)$ and $f_{\sim}(x_i, y_j)$, respectively. In this method, the best match between experimental and calculated images will be found by maximizing C_{corr}.

The main difficulty for these approaches is the preparation of two compared images, because experimentally recorded images are not always in the same orientation and magnification as simulated images. In practice, to bring the gray value of experimental images to the same scale as that of simulated images, we also need to record the maximum value and background level when conducting experiments.

5.2.2 Other programs

As discussed in Chapter 2 the phase shift generated by a single Ta atom at a radius of 0.1Å and a beam energy of 200keV is not small enough, thus a single tantalum atom is not a good weak phase object, which might cause the weak phase object approximation break down for our multiclice calculations. Even though we still got many reasonable matching results for CBED patterns of 1T-TaS_2 (see Chapter 4). However further quantitative analyses require more accurate methods to calculate electron micrograghs.

Another issue with multislice calculation for CBED patterns is the "expensive" running time. In our case a 1024×1024 pixel^2 CBED pattern with 16 phonon configurations for 26 layers of 1T-TaS_2 can take up to 8 hours. Improving the performance of computers is an option but other algorithms (Bloch-wave simulations) should be considered first.

5.2.3 Further study of CDW phases

As covered in Chapter 2, further aims of our work would involve understanding the influence of different stacking sequences on CDW phases of 1T-TaS_2. The potential application would be manipulating electron properties of 1T-TaS_2 via tuning the material's structure in three-dimension: CDW phases in (001) projection plane, and different thicknesses and stacking sequences along the z-axis.

APPENDIX A

ALL CONFIGURATIONS OF STACKING SEQUENCES

This chapter will discuss all configurations for stacking sequences of 1T-TaS_2 under ten layers.

Table A.1: All configurations of stacking sequences for three-layer 1T-TaS_2.

AAA			AAB			ABC		
Site 1	Site 2	Site 3	Site 1	Site 2	Site 3	Site 1	Site 2	Site 3
Ta	S	S	Ta	S	S	Ta	S	S
Ta	S	S	Ta	S	S	S	Ta	S
Ta	S	S	S	Ta	S	S	S	Ta

Table A.2: All configurations of stacking sequences for four-layer 1T-TaS_2.

AAAA			AAAB			AABB			AABC		
Site1	Site2	Site3	Site1	Site2	Site3	Site1	Site2	Site3	Site1	Site2	Site3
Ta	S	S	Ta	S	S	Ta	S	S	Ta	S	S
Ta	S	S	Ta	S	S	Ta	S	S	Ta	S	S
Ta	S	S	Ta	S	S	S	Ta	S	S	Ta	S
Ta	S	S	S	Ta	S	S	Ta	S	S	S	Ta

Table A.3: All configurations of stacking sequences for five-layer 1T-TaS_2.

AAAAA			AAAAB			AAABB			AAABC		
Site1	Site2	Site3	Site1	Site2	Site3	Site1	Site2	Site3	Site1	Site2	Site3
Ta	S	S	Ta	S	S	Ta	S	S	Ta	S	S
Ta	S	S	Ta	S	S	Ta	S	S	Ta	S	S
Ta	S	S	Ta	S	S	Ta	S	S	Ta	S	S
Ta	S	S	Ta	S	S	S	Ta	S	S	Ta	S
Ta	S	S	S	Ta	S	S	Ta	S	S	S	Ta

AABBC		
Site1	Site2	Site3
Ta	S	S
Ta	S	S
S	Ta	S
S	Ta	S
S	S	Ta

Table A.4: All configurations of stacking sequences for six-layer 1T-TaS_2.

AAAAAA			AAAAAB			AAAABB			AAAABC		
Site1	Site2	Site3	Site1	Site2	Site3	Site1	Site2	Site3	Site1	Site2	Site3
Ta	S	S	Ta	S	S	Ta	S	S	Ta	S	S
Ta	S	S	Ta	S	S	Ta	S	S	Ta	S	S
Ta	S	S	Ta	S	S	Ta	S	S	Ta	S	S
Ta	S	S	Ta	S	S	Ta	S	S	Ta	S	S
Ta	S	S	Ta	S	S	S	Ta	S	S	Ta	S
Ta	S	S	S	Ta	S	S	Ta	S	S	S	Ta
AAABBC			AAABBB			AABBCC					
Site1	Site2	Site3	Site1	Site2	Site3	Site1	Site2	Site3			
Ta	S	S	Ta	S	S	Ta	S	S			
Ta	S	S	Ta	S	S	Ta	S	S			
Ta	S	S	Ta	S	S	S	Ta	S			
S	Ta	S	S	Ta	S	S	Ta	S			
S	Ta	S	S	Ta	S	S	S	Ta			
S	S	Ta	S	Ta	S	S	S	Ta			

Table A.5: All configurations of stacking sequences for seven-layer 1T-TaS_2.

AAAAAAA			AAAAAAB			AAAAABB			AAAAABC		
Site1	Site2	Site3	Site1	Site2	Site3	Site1	Site2	Site3	Site1	Site2	Site3
Ta	S	S	Ta	S	S	Ta	S	S	Ta	S	S
Ta	S	S	Ta	S	S	Ta	S	S	Ta	S	S
Ta	S	S	Ta	S	S	Ta	S	S	Ta	S	S
Ta	S	S	Ta	S	S	Ta	S	S	Ta	S	S
Ta	S	S	Ta	S	S	Ta	S	S	Ta	S	S
Ta	S	S	Ta	S	S	S	Ta	S	S	Ta	S
Ta	S	S	S	Ta	S	S	Ta	S	S	S	Ta
AAAABBC			AAAABBB			AAABBCC			AAABBBC		
Site1	Site2	Site3	Site1	Site2	Site3	Site1	Site2	Site3	Site1	Site2	Site3
Ta	S	S	Ta	S	S	Ta	S	S	Ta	S	S
Ta	S	S	Ta	S	S	Ta	S	S	Ta	S	S
Ta	S	S	Ta	S	S	Ta	S	S	Ta	S	S
Ta	S	S	Ta	S	S	S	Ta	S	S	Ta	S
S	Ta	S	S	Ta	S	S	Ta	S	S	Ta	S
S	Ta	S	S	Ta	S	S	S	Ta	S	Ta	S
S	S	Ta	S	Ta	S	S	S	Ta	S	S	Ta

Table A.6: All configurations of stacking sequences for eight-layer 1T-TaS_2.

AAAAAAAA			AAAAAAAB			AAAAAABB			AAAAAABC		
Site1	Site2	Site3	Site1	Site2	Site3	Site1	Site2	Site3	Site1	Site2	Site3
Ta	S	S	Ta	S	S	Ta	S	S	Ta	S	S
Ta	S	S	Ta	S	S	Ta	S	S	Ta	S	S
Ta	S	S	Ta	S	S	Ta	S	S	Ta	S	S
Ta	S	S	Ta	S	S	Ta	S	S	Ta	S	S
Ta	S	S	Ta	S	S	Ta	S	S	Ta	S	S
Ta	S	S	Ta	S	S	Ta	S	S	Ta	S	S
Ta	S	S	Ta	S	S	S	Ta	S	S	Ta	S
Ta	S	S	S	Ta	S	S	Ta	S	S	S	Ta

AAAAABBC			AAAAABBB			AAAABBCC			AAAABBBC		
Site1	Site2	Site3	Site1	Site2	Site3	Site1	Site2	Site3	Site1	Site2	Site3
Ta	S	S	Ta	S	S	Ta	S	S	Ta	S	S
Ta	S	S	Ta	S	S	Ta	S	S	Ta	S	S
Ta	S	S	Ta	S	S	Ta	S	S	Ta	S	S
Ta	S	S	Ta	S	S	Ta	S	S	Ta	S	S
Ta	S	S	Ta	S	S	S	Ta	S	S	Ta	S
S	Ta	S	S	Ta	S	S	Ta	S	S	Ta	S
S	Ta	S	S	Ta	S	S	S	Ta	S	Ta	S
S	S	Ta	S	Ta	S	S	S	Ta	S	S	Ta
AAABBBCC			AAAABBBB								
Site1	Site2	Site3	Site1	Site2	Site3						
Ta	S	S	Ta	S	S						
Ta	S	S	Ta	S	S						
Ta	S	S	Ta	S	S						
S	Ta	S	Ta	S	S						
S	Ta	S	S	Ta	S						
S	Ta	S	S	Ta	S						
S	S	Ta	S	Ta	S						
S	S	Ta	S	Ta	S						

Table A.7: All configurations of stacking sequences for nine-layer 1T-TaS_2.

AAAAAAAAA			AAAAAAAAB			AAAAAAABB			AAAAAAABC		
Site1	Site2	Site3	Site1	Site2	Site3	Site1	Site2	Site3	Site1	Site2	Site3
Ta	S	S	Ta	S	S	Ta	S	S	Ta	S	S
Ta	S	S	Ta	S	S	Ta	S	S	Ta	S	S
Ta	S	S	Ta	S	S	Ta	S	S	Ta	S	S
Ta	S	S	Ta	S	S	Ta	S	S	Ta	S	S
Ta	S	S	Ta	S	S	Ta	S	S	Ta	S	S
Ta	S	S	Ta	S	S	Ta	S	S	Ta	S	S
Ta	S	S	Ta	S	S	Ta	S	S	Ta	S	S
Ta	S	S	Ta	S	S	S	Ta	S	S	Ta	S
Ta	S	S	S	Ta	S	S	Ta	S	S	S	Ta
AAAAAABBC			AAAAAABBB			AAAAABBCC			AAAAABBBC		
Site1	Site2	Site3	Site1	Site2	Site3	Site1	Site2	Site3	Site1	Site2	Site3
Ta	S	S	Ta	S	S	Ta	S	S	Ta	S	S
Ta	S	S	Ta	S	S	Ta	S	S	Ta	S	S
Ta	S	S	Ta	S	S	Ta	S	S	Ta	S	S
Ta	S	S	Ta	S	S	Ta	S	S	Ta	S	S
Ta	S	S	Ta	S	S	Ta	S	S	Ta	S	S
Ta	S	S	Ta	S	S	S	Ta	S	S	Ta	S
S	Ta	S	S	Ta	S	S	Ta	S	S	Ta	S
S	Ta	S	S	Ta	S	S	S	Ta	S	Ta	S
S	S	Ta	S	Ta	S	S	S	Ta	S	S	Ta
AAAAABBBB			AAAABBBBC			AAAABBBCC			AAABBBCCC		
Site1	Site2	Site3	Site1	Site2	Site3	Site1	Site2	Site3	Site1	Site2	Site3
Ta	S	S	Ta	S	S	Ta	S	S	Ta	S	S
Ta	S	S	Ta	S	S	Ta	S	S	Ta	S	S
Ta	S	S	Ta	S	S	Ta	S	S	Ta	S	S
Ta	S	S	Ta	S	S	Ta	S	S	S	Ta	S
Ta	S	S	S	Ta	S	S	Ta	S	S	Ta	S
S	Ta	S	S	Ta	S	S	Ta	S	S	Ta	S

S	Ta	S	S	Ta	S	S	Ta	S	S	S	Ta
S	Ta	S	S	Ta	S	S	S	Ta	S	S	Ta
S	Ta	S	S	S	Ta	S	S	Ta	S	S	Ta

Table A.8: All configurations of stacking sequences for ten-layer 1T-TaS_2.

AAAAAAAAAA			AAAAAAAAAB			AAAAAAAABB			AAAAAAAABC		
Site1	Site2	Site3	Site1	Site2	Site3	Site1	Site2	Site3	Site1	Site2	Site3
Ta	S	S	Ta	S	S	Ta	S	S	Ta	S	S
Ta	S	S	Ta	S	S	Ta	S	S	Ta	S	S
Ta	S	S	Ta	S	S	Ta	S	S	Ta	S	S
Ta	S	S	Ta	S	S	Ta	S	S	Ta	S	S
Ta	S	S	Ta	S	S	Ta	S	S	Ta	S	S
Ta	S	S	Ta	S	S	Ta	S	S	Ta	S	S
Ta	S	S	Ta	S	S	Ta	S	S	Ta	S	S
Ta	S	S	Ta	S	S	Ta	S	S	Ta	S	S
Ta	S	S	Ta	S	S	S	Ta	S	S	Ta	S
Ta	S	S	S	Ta	S	S	Ta	S	S	S	Ta
AAAAAAABBC			AAAAAAABBB			AAAAAABBCC			AAAAAABBBC		
Site1	Site2	Site3	Site1	Site2	Site3	Site1	Site2	Site3	Site1	Site2	Site3
Ta	S	S	Ta	S	S	Ta	S	S	Ta	S	S
Ta	S	S	Ta	S	S	Ta	S	S	Ta	S	S
Ta	S	S	Ta	S	S	Ta	S	S	Ta	S	S
Ta	S	S	Ta	S	S	Ta	S	S	Ta	S	S
Ta	S	S	Ta	S	S	Ta	S	S	Ta	S	S
Ta	S	S	Ta	S	S	Ta	S	S	Ta	S	S
Ta	S	S	Ta	S	S	S	Ta	S	S	Ta	S
S	Ta	S	S	Ta	S	S	Ta	S	S	Ta	S
S	Ta	S	S	Ta	S	S	S	Ta	S	Ta	S
S	S	Ta	S	Ta	S	S	S	Ta	S	S	Ta
AAAAAABBBB			AAAAABBBBC			AAAAABBBCC			AAAABBBCCC		
Site1	Site2	Site3	Site1	Site2	Site3	Site1	Site2	Site3	Site1	Site2	Site3
Ta	S	S	Ta	S	S	Ta	S	S	Ta	S	S
Ta	S	S	Ta	S	S	Ta	S	S	Ta	S	S
Ta	S	S	Ta	S	S	Ta	S	S	Ta	S	S
Ta	S	S	Ta	S	S	Ta	S	S	Ta	S	S
Ta	S	S	Ta	S	S	Ta	S	S	S	Ta	S
Ta	S	S	S	Ta	S	S	Ta	S	S	Ta	S
S	Ta	S	S	Ta	S	S	Ta	S	S	Ta	S
S	Ta	S	S	Ta	S	S	Ta	S	S	S	Ta
S	Ta	S	S	Ta	S	S	S	Ta	S	S	Ta
S	Ta	S	S	S	Ta	S	S	Ta	S	S	Ta
AAAAABBBBB			AAAABBBBCC								
Site1	Site2	Site3	Site1	Site2	Site3						
Ta	S	S	Ta	S	S						
Ta	S	S	Ta	S	S						
Ta	S	S	Ta	S	S						
Ta	S	S	Ta	S	S						
Ta	S	S	S	Ta	S						
S	Ta	S	S	Ta	S						
S	Ta	S	S	Ta	S						
S	Ta	S	S	Ta	S						
S	Ta	S	S	S	Ta						

S	Ta	S	S	S	Ta

APPENDIX B

LINEAR IMAGING MODEL

In this section we will briefly discuss an approximate linear imaging model for thin specimens.

If the wavefunction of the focused probe is described as $\psi_p(\mathbf{x})$, then the point spread function is just:

$$\psi_{\mathrm{psf}}(\mathbf{x}) = \left|\psi_p(\mathbf{x})\right|^2 = \left|\int_0^{k_{\max}} \exp[-\mathrm{i}\chi(\mathbf{k}) - 2\pi\mathrm{i}\mathbf{k}\cdot\mathbf{x}]\mathrm{d}^2\mathbf{k}\right|^2,$$

where $\chi(\mathbf{k})$ is the aberration function.

In our approximation, the specimen function $\psi_s(\mathbf{x})$ represents the probability of electron scattering to angle k_s on the ADF detector. Then we have:

$$\psi_s(\mathbf{x}) \sim \int_{k_{D\min}}^{k_{D\max}} \frac{\partial\sigma(\mathbf{x})}{\partial k_s}\mathrm{d}^2 k_s\,,$$

where $\frac{\partial\sigma(\mathbf{x})}{\partial k_s}$, the square of scattering factor $f_e(\mathbf{q})$, is the partial cross section corresponding to scattering angles k_s, and scattering factors can be calculated in the first Born approximation [23].

Thus, the transmitted intensity is simply the convolution of the specimen function and the point spread function:

$$I(\mathbf{x}) = \psi_{\mathrm{psf}}(\mathbf{x}) \otimes \psi_s(\mathbf{x}).$$

REFERENCE

[1] Möbus, G., & Rühle, M. (1994). Structure determination of metal-ceramic interfaces by numerical contrast evaluation of HRTEM micrographs. *Ultramicroscopy*, *56*(1), 54-70.

[2] Mak, K. F., Lee, C., Hone, J., Shan, J., & Heinz, T. F. (2010). Atomically thin MoS_2: a new direct-gap semiconductor. *Physical Review Letters*, *105*(13), 136805.

[3] Radisavljevic, B., Radenovic, A., Brivio, J., Giacometti, V., & Kis, A. (2011). Single-layer MoS_2 transistors. *Nature nanotechnology*, *6*(3), 147-150.

[4] Bhattacharyya, S., & Singh, A. K. (2012). Semiconductor-metal transition in semiconducting bilayer sheets of transition-metal dichalcogenides. *Physical Review B*, *86*(7), 075454.

[5] Li, L. J., Lu, W. J., Zhu, X. D., Ling, L. S., Qu, Z., & Sun, Y. P. (2012). Fe-doping–induced superconductivity in the charge-density-wave system 1T-TaS_2. *EPL (Europhysics Letters)*, *97*(6), 67005.

[6] Sipos, B., Kusmartseva, A. F., Akrap, A., Berger, H., Forró, L., & Tutiš, E. (2008). From Mott state to superconductivity in 1T-TaS_2. *Nature materials*, *7*(12), 960-965.

[7] Liu, Y., Ang, R., Lu, W. J., Song, W. H., Li, L. J., & Sun, Y. P. (2013). Superconductivity induced by Se-doping in layered charge-density-wave system 1T-$TaS_{2-x}Se_x$. *Applied Physics Letters*, *102*(19), 192602.

[8] Yu, Y., Yang, F., Lu, X. F., Yan, Y. J., Cho, Y. H., Ma, L. & Zhang, Y. (2015). Gate-tunable phase transitions in thin flakes of 1T-TaS_2. *Nature nanotechnology*, *10*(3), 270-276.

[9] Kourkoutis, L. F., Parker, M. K., Vaithyanathan, V., Schlom, D. G., & Muller, D. A. (2011). Direct measurement of electron channeling in a crystal using scanning transmission electron microscopy. *Physical Review B*, *84*(7), 075485.

[10] LeBeau, J. M., Findlay, S. D., Allen, L. J., & Stemmer, S. (2010). Position averaged convergent beam electron diffraction: Theory and applications.*Ultramicroscopy*, *110*(2), 118-125.

[11] Wu, R. J., Odlyzko, M. L., & Mkhoyan, K. A. (2014). Determining the thickness of atomically thin MoS_2 and WS_2 in the TEM. *Ultramicroscopy*, *147*, 8-20.

[12] Hwang, J., Zhang, J. Y., Son, J., & Stemmer, S. (2012). Nanoscale quantification of octahedral tilts in perovskite films. *Applied Physics Letters*,*100*(19), 191909.

[13] Jariwala, D., Sangwan, V. K., Lauhon, L. J., Marks, T. J., & Hersam, M. C. (2014). Emerging device applications for semiconducting two-dimensional transition metal dichalcogenides. *ACS nano*, *8*(2), 1102-1120.

[14] Janssen, T., & Janner, A. (1987). Incommensurability in crystals. *Advances in Physics*, *36*(5), 519-624.

[15] Tsen, A. W., Hovden, R., Wang, D. Z., Kim, Y. D., Okamoto, J., Spoth, K. A., ... & Pasupathy, A. N. (2015). Structure and Control of Charge Density Waves in Two-Dimensional 1T-TaS_2. *arXiv preprint arXiv:1505.03769*.

[16] Walker, M. B., & Withers, R. L. (1983). Stacking of charge-density waves in 1 T transition-metal dichalcogenides. *Physical Review B*, *28*(5), 2766.

[17] Williams, P. M., Scruby, C., Clark, W., & Parry, G. (1976). Charge density waves in the layered transition metal dichalcogenides. *Journal de Physique Colloques*, *37*(C4), C4-139.

[18] Bovet, M., van Smaalen, S., Berger, H., Gaal, R., Forró, L., Schlapbach, L., & Aebi, P. (2003). Interplane coupling in the quasi-two-dimensional 1T−TaS_2.*Physical Review B*, *67*(12), 125105.

[19] Scherzer, O. (1949). The theoretical resolution limit of the electron microscope.*Journal of Applied Physics*, *20*(1), 20-29.

[20] Krivanek, O. L., Ursin, J. P., Bacon, N. J., Corbin, G. J., Dellby, N., Hrncirik, P., ... & Szilagyi, Z. S. (2009). High-energy-resolution monochromator for aberration-

corrected scanning transmission electron microscopy/electron energy-loss spectroscopy. *Philosophical Transactions of the Royal Society of London A: Mathematical, Physical and Engineering Sciences*, *367*(1903), 3683-3697.

[21] LeBeau, J. M., Findlay, S. D., Wang, X., Jacobson, A. J., Allen, L. J., & Stemmer, S. (2009). High-angle scattering of fast electrons from crystals containing heavy elements: Simulation and experiment. *Physical Review B*,*79*(21), 214110.

[22] Cowley, J. T., & Iijima, S. (1972). Electron Microscope Image Contrast for Thin Crystal. *Zeitschrift für Naturforschung A*, *27*(3), 445-451.

[23] Kirkland, E. J. (2010). *Advanced computing in electron microscopy*. Springer Science & Business Media.

[24] Spijkerman, A., de Boer, J. L., Meetsma, A., Wiegers, G. A., & van Smaalen, S. (1997). X-ray crystal-structure refinement of the nearly commensurate phase of $1T-TaS_2$ in (3+2)-dimensional superspace. *Physical Review B*, *56*(21), 13757.

[25] Jellinek, F. (1962). The system tantalum-sulfur. *Journal of the Less Common Metals*, *4*(1), 9-15.

[26] Kittel, C. (2005). *Introduction to solid state physics*. Wiley.

[27] Loane, R. F., Xu, P., & Silcox, J. (1991). Thermal vibrations in convergent-beam electron diffraction. *Acta Crystallographica Section A: Foundations of Crystallography*, *47*(3), 267-278.

[28] Hillyard, S., & Silcox, J. (1994, January). Annular dark field imaging in STEM. In *MRS Proceedings* (Vol. 332, p. 361). Cambridge University Press.

[29] Hsieh, S. M., & Colella, R. (1987). Dimensional effects of Debye-Waller factors in layered crystals. *Solid state communications*, *63*(1), 47-50.

[30] Fitting, L., Thiel, S., Schmehl, A., Mannhart, J., & Muller, D. A. (2006). Subtleties in ADF imaging and spatially resolved EELS: A case study of low-angle twist boundaries in $SrTiO_3$. *Ultramicroscopy*, *106*(11), 1053-1061.

[31] Kirkland, E. J., Loane, R. F., & Silcox, J. (1987). Simulation of annular dark field STEM images using a modified multislice method. *Ultramicroscopy*, *23*(1), 77-96.

[32] Loane, R. F., Xu, P., & Silcox, J. (1992). Incoherent imaging of zone axis crystals with ADF STEM. *Ultramicroscopy*, *40*(2), 121-138.

[33] Loane, R. F., Kirkland, E. J., & Silcox, J. (1988). Visibility of single heavy atoms on thin crystalline silicon in simulated annular dark-field STEM images.*Acta Crystallographica Section A: Foundations of Crystallography*, *44*(6), 912-927.

[34] Weyland, M., & Muller, D. A. (2005). Tuning the convergence angle for optimum STEM performance. *FEI Nanosolutions*, *1*, 24-35.

[35] Barry, J. C. (1992). Image-matching as a means of atomic structure evaluation in high resolution transmission electron microscopy. *SCANNING MICROSCOPY-SUPPLEMENT-*, 209-209.

[36] Barry, J. C. (1989). Semiquantitative image matching in HRTEM. *Computer Simulation of Electron Microscope Diffraction and Images*, 57-78.

[37] Thust, A., & Urban, K. (1992). Quantitative high-speed matching of high-resolution electron microscopy images. *Ultramicroscopy*, *45*(1), 23-42.

[38] Möbus, G., & Rühle, M. (1994). Structure determination of metal-ceramic interfaces by numerical contrast evaluation of HRTEM micrographs.*Ultramicroscopy*, *56*(1), 54-70.